REVIEW

National Science Review
1: 371–395, 2014
doi: 10.1093/nsr/nwu007
Advance access publication 3 July 2014

PHYSICS

Iron-based high transition temperature superconductors

Xianhui Chen[1], Pengcheng Dai[2,3], Donglai Feng[4], Tao Xiang[3,5] and Fu-Chun Zhang[6,*]

ABSTRACT

In a superconductor electrons form pairs and electric transport becomes dissipation-less at low temperatures. Recently discovered iron-based superconductors have the highest superconducting transition temperature next to copper oxides. In this article, we review material aspects and physical properties of iron-based superconductors. We discuss the dependence of transition temperature on the crystal structure, the interplay between antiferromagnetism and superconductivity by examining neutron scattering experiments, and the electronic properties of these compounds obtained by angle-resolved photoemission spectroscopy in link with some results from scanning tunneling microscopy/spectroscopy measurements. Possible microscopic model for this class of compounds is discussed from a strong coupling point of view.

Keywords: superconductivity, angle-resolved photoemission spectroscopy, iron-based superconductors

[1]Department of Physics, University of Science and Technology of China, Hefei 230026, China, [2]Department of Physics and Astronomy, Rice University, Houston, TX 77005, USA, [3]Institute of Physics, Chinese Academy of Sciences, Beijing 100190, China, [4]Department of Physics, Fudan University, Shanghai 200433, China, [5]Collaborative Innovation Center of Quantum Matter, Beijing 100190, China and [6]Department of Physics, Zhejiang University, Hangzhou 310027, China

***Corresponding author**. E-mail: fuchun@hku.hk

Received 1 March 2014; **Revised** 31 March 2014; **Accepted** 8 April 2014

INTRODUCTION

Superconductivity is a remarkable macroscopic quantum phenomenon, which was discovered by Kamerlingh Onnes in 1911. As temperature decreases to below a critical value, electric resistance of a superconductor vanishes and the magnetic field is repelled. Superconductors have many applications. As an example, magnetic resonance imaging has been widely used in medical facilities. Superconductors may be used to transport electricity without loss of energy. Conventional superconductivity is well explained by Bardeen–Cooper–Schrieffer (BCS) theory, which was established in 1957. In a superconducting (SC) state, two electrons with opposite momenta attract each other to form a bound pair. The pairing mechanism in a conventional superconductor is due to couplings between electrons and phonons, which are quantum version of lattice vibration. The transition temperatures (T_cs) are, however, very low, and usually well below 40 K. The low transition temperature has greatly limited practical applications of superconductors. It has been a dream to realize high-T_c or room temperature superconductors, which may revolutionarily change the power transmission in the world.

There was a great excitement after the discovery of high-T_c SC cuprate by Bednorz and Müller in 1986, who reported T_c well above 30 K in $La_{2-x}Ca_xCuO_4$ [1]. The subsequent world-wide efforts in search of high-T_c SC cuprate raised the transition temperature beyond the liquid nitrogen temperature of 77 K for the first time [2] and the highest T_c at ambient pressure is 135 K in Hg-based cuprates, which remains the record as of today. All the cuprates share a common structure element CuO_2 plane, where Cu atoms form a square lattice. The second class of high-T_c materials are iron-based superconductors, which were discovered by Hosono and co-workers in early 2008 [3], who reported $T_c = 26$ K in LaOFeAs with part of O atoms replaced by F atoms. Soon after this discovery, the transition temperature has been raised to above 40 K at ambient pressure by substitution of different elements [4–7]. The highest T_c in bulk iron-based superconductors is 55 K in $SmO_{1-x}F_xFeAs$ reported by Ren *et al.* [6], and similarly in $Gd_{1-x}Th_xFeAsO$ [8]. So far many families of iron-based superconductors have been discovered [9–13]. Most recently, monolayer FeSe superconductivity on top of substrate $SrTiO_3$ has been reported [14], and there is an indication that T_c is likely higher than the bulk ones.

Study of iron-based superconductors and their physical properties has been one of the major activities in condensed matter physics in the past several

years. At the time when the iron-based superconductor was discovered, scientists in the field of superconductivity were well prepared. Several powerful new techniques, such as angle-resolved photoemission spectroscope (ARPES) and scanning tunneling microscopy (STM), have been well developed during the course of studying high-T_c cuprates. These techniques together with some more conventional techniques, such as neutron scattering, nuclear magnetic resonance (NMR), and optical conducting measurements, have been applied to examine the properties of the new compounds. Iron-based superconductivity shares many common features with the high-T_c cuprates. Both of them are unconventional superconductors in the sense that phonons unlikely play any dominant role in their superconductivity. Both are quasi-2D, and their superconductivity is in the proximity of antiferromagnetism. On the other hand, iron-based superconductors have a number of distinct properties from the cuprates. The parent compounds of the SC cuprates are antiferromagnetic (AF) Mott insulators due to strong Coulomb repulsion, and the lightly doped superconductors are doped Mott insulators [15–18]. On the other hand, the parent compounds of iron-based superconductors are semi-metallic. Dynamic mean field calculations indicate that the iron-based compounds are close to metal–insulator transition line but are at the metallic side [19]. In the curpates, the low-energy physics is described by a single band [20], while in the iron-based compounds, there are multi-orbitals involved. Despite over 25 years of study, some of the physics in the cuprates remain controversial. The investigation of iron-based superconductors may help us to understand the unconventional superconductivity and also provide a new route for searching higher temperature superconductors.

The purpose of this article is to provide an overall picture of the iron-based superconductivity based on our present understanding. Instead of giving a broad review to cover all the experimental and theoretical developments in this field, we will discuss basic physical properties of the materials and the underlying physics by examining limited experiments and theories. We refer the readers to several recent review papers [21–27] for more complete description of the field. The rest of the article is organized as follows. In the 'Materials and crystal structures' section, we discuss material aspects of the compounds. Antiferromagnetism and superconductivity will be discussed in the 'The interplay between magnetism and superconductivity' section. In the 'Electronic properties' section, we discuss electronic structure of iron-based materials largely based on ARPES and STM experiments. We briefly present our theoretical understanding of the electronic structure and superconductivity in the 'Theory' section. The article will end with a summary and perspective.

MATERIALS AND CRYSTAL STRUCTURES

Material classification and crystal structures

Substitution of magnetic Sm for non-magnetic La leads to a dramatic increase in T_c from 26 K in $LaFeAsO_{1-x}F_x$ to 43 K in $SmFeAsO_{1-x}F_x$ [3,4]. This suggests that a higher T_c is possibly realized in the layered oxypnictides. The achieved T_c of 43 K in $SmFeAsO_{1-x}F_x$ is higher than the commonly believed upper limit (40 K) of electron–phonon-mediated superconductors, which gives pieces of compelling evidence for classifying layered iron-based superconductors as a family of unconventional superconductors. Subsequently, many new iron-based superconductors with diverse crystal structures were found and they can be categorized into several families according to their structural features.

The iron-based superconductors share the common Fe_2X_2 (X = As and Se)-layered structure unit, which possesses an anti-PbO-type (anti-litharge-type) atom arrangement. The Fe_2X_2 layers consist of edge-shared $FeX_{4/4}$ tetrahedra, which has $\bar{4}m2$ site symmetry. In the Fe_2X_2 layers, X ions form a distorted tetrahedral arrangement around the Fe ions, giving rise to two distinct X-Fe-X bond angles with multiplicities of two and four which we refer to as α and β, respectively.

FeSe (T_c = 8 K) has the simplest structure among the known iron-based superconductors, which is called 11 phase [11]. FeSe is formed by alternate stacking of the anti-PbO FeSe layers. In FeSe, the cations and anions occupy the opposite sites to Pb and O atoms of litharge, so that we call it anti-PbO or anti-litharge structure. FeSe adopts a space group of P4/nmm. The Fe_2Se_2 monolayer consists of flat Fe_2 square-net sandwiched by two Se monolayers. Consequently, each Fe atom is coordinated with four Se atoms to establish the edge-shared $FeSe_4$ tetrahedron, forming a 2D square-net Fe_2Se_2 monolayer. As shown in Fig. 1, these tetrahedral Fe_2X_2 layers can be separated by alkali and alkali-earth cations, LnO layers or perovskite-related oxydic slabs. Fig. 1 also illustrates the crystal structures of AFeAs, $AeFe_2As_2$, and LnOFeAs. Their basic crystallographic data are listed in Table 1. The simplest FeAs-based superconductor in structure is the AFeAs (A = Li and Na, called 111 phase) [12,13,28]. AFeAs crystallizes in an anti-PbFCl-type structure, which adopts a Cu_2Sb

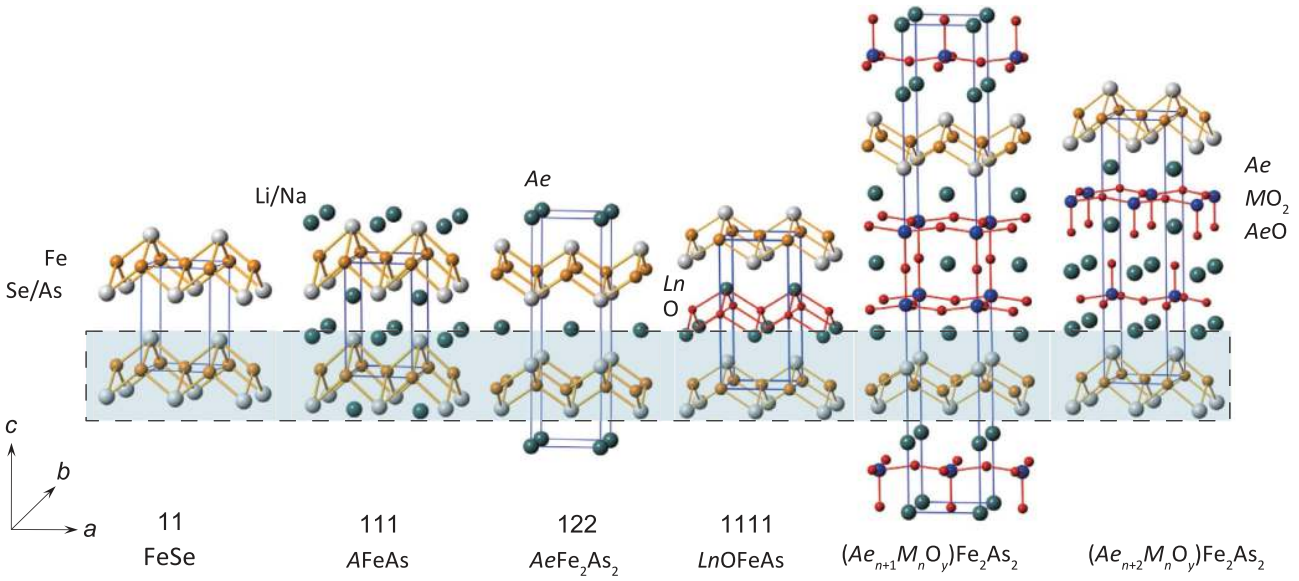

Figure 1. The schematic view of the crystal structures for several typical types of iron-based superconductors, in which A, Ae, Ln, and M stand for alkali, alkali-earth, lanthanide, and transition metal atoms.

Table 1. Maximum temperatures of the SC transition under ambient pressure and lattice parameters of undoped compounds for some typical iron pnictides.

Compound	Maximum T_c (K)	Space group	a (Å)	c (Å)	Ref.
LiFeAs	18	P4/nmm	3.775	6.353	[4]
$BaFe_2As_2$	38	I4/mmm	3.963	13.017	[13]
LaOFeAs	41	P4/nmm	4.035	8.740	[24]
CeOFeAs	41	P4/nmm	3.996	8.648	[24]
PrOFeAs	52	P4/nmm	3.926	8.595	[24]
NdOFeAs	51.9	P4/nmm	3.940	8.496	[24]
SmOFeAs	55	P4/nmm	3.940	8.496	[24]
GdOFeAs	53.5	P4/nmm	3.915	8.435	[24]
TbOFeAs	48.5	P4/nmm	3.898	8.404	[24]

(or Fe_2As) structure. AFeAs has the space group of P4/nmm and each unit cell includes two chemical formula, that is 2A, 2Fe, and 2As. Fe and As are arranged in anti-PbO-type layers with double Li/Na planes located between the layers in square-based pyramidal coordination by As.

With additional atoms added into the anti-PbFCl-type structure, we can achieve ZrCuSiAs-type 1111 superconductors. Up to now, the highest $T_c \sim 55$ K in iron-based superconductors has been achieved in fluorine-doped or oxygen-deficient LnFeAsO compounds (Ln represents rare-earth metal atoms) [6], which are usually briefly written as 1111 phase. LnFeAsO compounds have a tetragonal layered structure at room temperature, with space group P4/nmm. The schematic view of their crystal structure is shown in Fig. 1. The earliest discovered 1111 compound with relatively high T_c is LaFeAsO [3], with lattice constants at room temperature $a = 4.032\,68(1)$ Å, $c = 8.741\,11(4)$ Å. For these 1111 compounds, their structure consists of alternate stacking of FeAs layers and fluorite-type LnO layers. For LaFeAsO, the distance between the adjacent FeAs and LaO layers is 1.8 Å. The lattice constants a and c decrease with reducing the ion radii of the rare-earth metals. With the decreasing radii of the rare-earth metal ions, the optimal T_c first increases rapidly, reaching the highest T_c (= 55 K) in the doped SmFeAsO system [6,29], and then decreases slightly with further reducing the radii of the rare-earth metal ions. Besides LnFeAsO systems, there are other types of 1111 FeAs-based compounds, AeFFeAs (Ae = Ca, Sr, and Ba) [30,31] and CaHFeAs [32]. AeFFeAs (Ae = Ca, Sr, and Ba) and CaHFeAs are also parent compounds of superconductors [33–35]. Very recently, a new 1111-type FeSe-derived superconductor, $LiFeO_2Fe_2Se_2$ with $T_c \approx 43$ K, was synthesized by Lu *et al.* [36].

The other typical type of compounds, $ThCr_2Si_2$-type iron arsenides, possess only single layers of separating spacer atoms between Fe_2X_2 (so-called 122 structure), which is adopted by $AeFe_2As_2$ (Ae = Ca, Sr, Ba, Eu, K, etc.) [10,37–39] and $A_xFe_{2-y}Se_2$ (A = K, Rb, Cs, Tl/K, and Tl/Rb) [40–43]. $AeFe_2As_2$ adopts body-centered tetragonal lattice and has space group of I4/mmm. In FeAs-122, the highest $T_c \sim 49$ K can be achieved in Pr-doped $CaFe_2As_2$ [44]. However, some recent reports revealed that such superconductivity with T_c higher than 40 K should be ascribed to a new structural

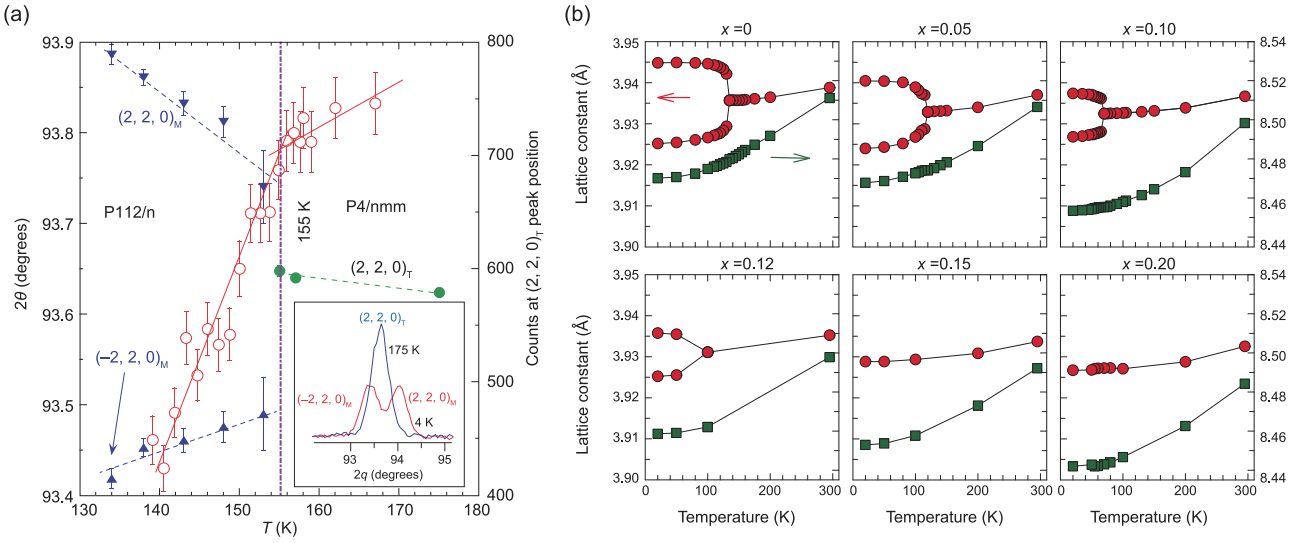

Figure 2. (a) Neutron scattering result on structural transitions on LaOFeAs [58]. (b) The temperature dependence of lattice constants for different F-doping levels in the $SmFeAsO_{1-x}F_x$ system.

phase (Ca,Ln)$FeAs_2$ (Ln = La, Pr). Crystal structure of (Ca,Ln)$FeAs_2$ is derived from $CaFe_2As_2$, with shifting the adjacent FeAs layers along the 45° direction of ab-plane by half lattice length on the basis of $CaFe_2As_2$, and then intercalating one additional As-plane and one Ca-plane for every two CaFeAs blocks [45]. FeSe-derived superconductors $A_xFe_{2-y}Se_2$ also crystallize in 122 structure, which have a T_c of ∼ 30 K in crystals grown by the high-temperature melting method [40–43] or higher than 40 K by co-intercalation of alkali atoms and certain molecules (NH_3 or organic) by a low-temperature solution route [46–49].

According to the previous knowledge in the high-T_c cuprates, superconductivity is closely related to the separating spacers between adjacent conducting layers. Therefore, compounds with complicated structures between FeAs layers were synthesized. Up to now, $Ae_{n+1}M_nO_yFe_2As_2$ and $Ae_{n+2}M_nO_yFe_2As_2$ [Ae = Ca, Sr, Ba; M = Sc, V, (Ti, Al), (Ti, Mg), and (Sc, Mg)] systems have been successfully synthesized, where $y \sim 3n-1$ for the former and $y \sim 3n$ for the latter [50–53]. Fig. 1 shows the crystal structures for the case of $n = 1$. They all adopt tetragonal lattice. All $Ae_{n+1}M_nO_yFe_2As_2$ compounds share the same space group of D_h^{17}-I4/mmm, while for $Ae_{n+2}M_nO_yFe_2As_2$, its space group is P4/nmm for $n = 2$ and 4, whereas P4mm for $n = 3$. For $Ae_{n+1}M_nO_yFe_2As_2$, n perovskite layers are sandwiched between adjacent FeAs layers, while for $Ae_{n+2}M_nO_yFe_2As_2$ there are n perovskite layers plus one rock-salt layer in each blocking layer. The $Ae_{n+2}M_nO_yFe_2As_2$ and $Ae_{n+2}M_nO_yFe_2As_2$ can be SC with T_c ranging from 17 to 47 K [52–54]. There are some other FeAs-based superconductors with quite complicated structures, such as Ca-Fe-Pt-As system $Ca_{10}(Pt_3As_8)(Fe_2As_2)_5$ (so-called 10-3-8), $Ca_{10}(Pt_4As_8)(Fe_2As_2)_5$ (so-called 10-4-8) [55,56], $Ba_2Ti_2Fe_2As_4O$ [57], and so on.

There is a resistivity anomaly in the parent compound of LaFeAsO at around 150 K, which disappears as superconductivity emerges [3]. It was clarified later by de la Curz *et al.* through neutron scattering experiment that such an anomaly around 155 K could be attributed to the structural phase transition [58]. As shown in Fig. 2, a structural transition occurs around 155 K in undoped LaOFeAs. The space group of the low-temperature structure was clarified to be the orthorhombic Cmma [59,60]. The space group changes from the high-temperature tetragonal P4/nmm to low-temperature orthorhombic Cmma, corresponding to a transformation from 5.703 07 Å × 5.703 07 Å square network (for comparison, here we use $a\sqrt{2}$, so that space group becomes F4/mmm) to 5.682 62 Å × 5.571 043 Å with a slight shrink of the c-axis lattice constant, as shown in the left panel of Fig. 2 [61]. In the structural transition, chemical formulae in each unit cell change from 2 to 4 with a symmetry degradation. With decreasing temperature, the parent and slightly doped $AeFe_2As_2$ (Ae = Ca, Sr, Ba, and Eu) also undergo a structural transition from high-temperature tetragonal phase to low-temperature orthorhombic phase. The low-temperature orthorhombic phase has the space group of Fmmm [10,62]. Fig. 3 shows that $FeAs_4$ tetrahedron distorts in the structural transition in $BaFe_2As_2$. The As-Fe-As angles around 108.7° become non-equivalent and evolve to two values of 108.1° and 108.7°, respectively [10]. Such

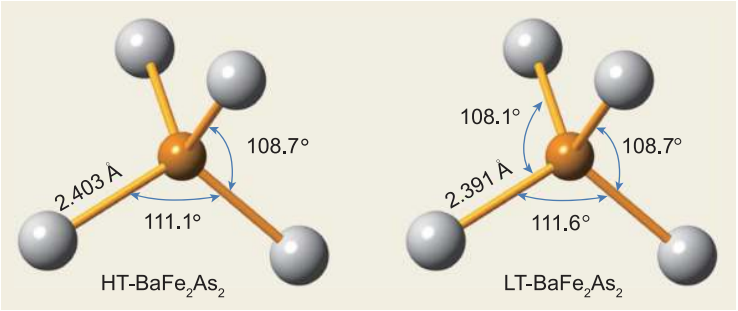

Figure 3. As-Fe-As bond angles of $BaFe_2As_2$ at high and low temperature, respectively (data from [10]).

a structural transition from high-temperature tetragonal symmetry to low-temperature orthorhombic symmetry occurs among the undoped and underdoped FeAs-based 111, 122, and 1111 phases.

Relation between crystal structure and superconductivity

By summarizing plenty of data about crystal structure and T_c for iron-based superconductors, it is found that T_c is related to structure parameters [63–65]. In particular, there is a close relation between the anion (As, P, Se, and Te) height from the Fe layer (h) and T_c, as shown in Fig. 4a [63]. h depends on the type of anion, increasing in turn from

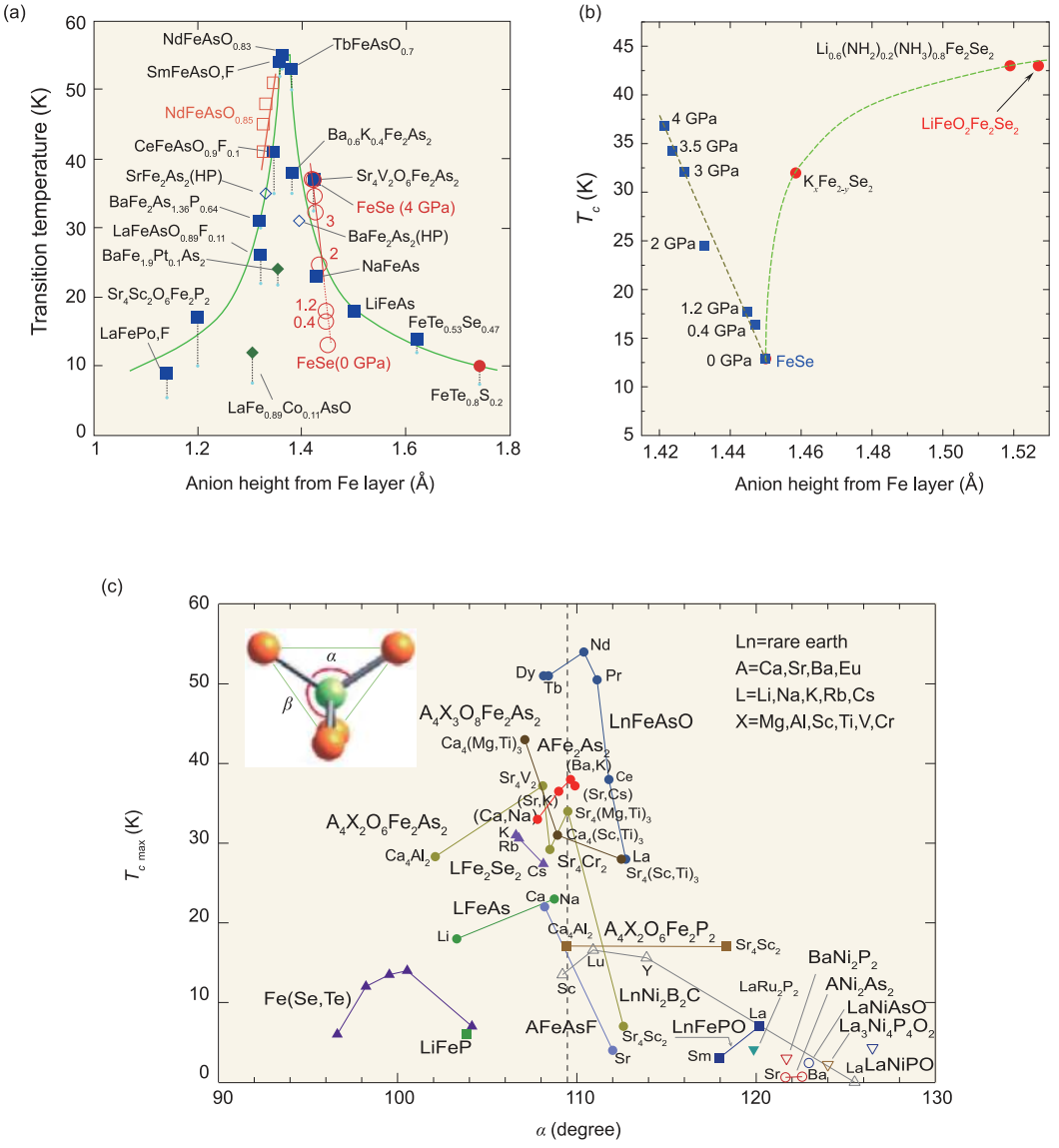

Figure 4. (a) Anion height dependence of T_c in iron-based superconductors [63]. (b) Anion height dependence of T_c in FeSe-derived superconductors [36]. (c) The relation between the As(top)-Fe-As(top) angle α and T_c of iron-based superconductors [64].

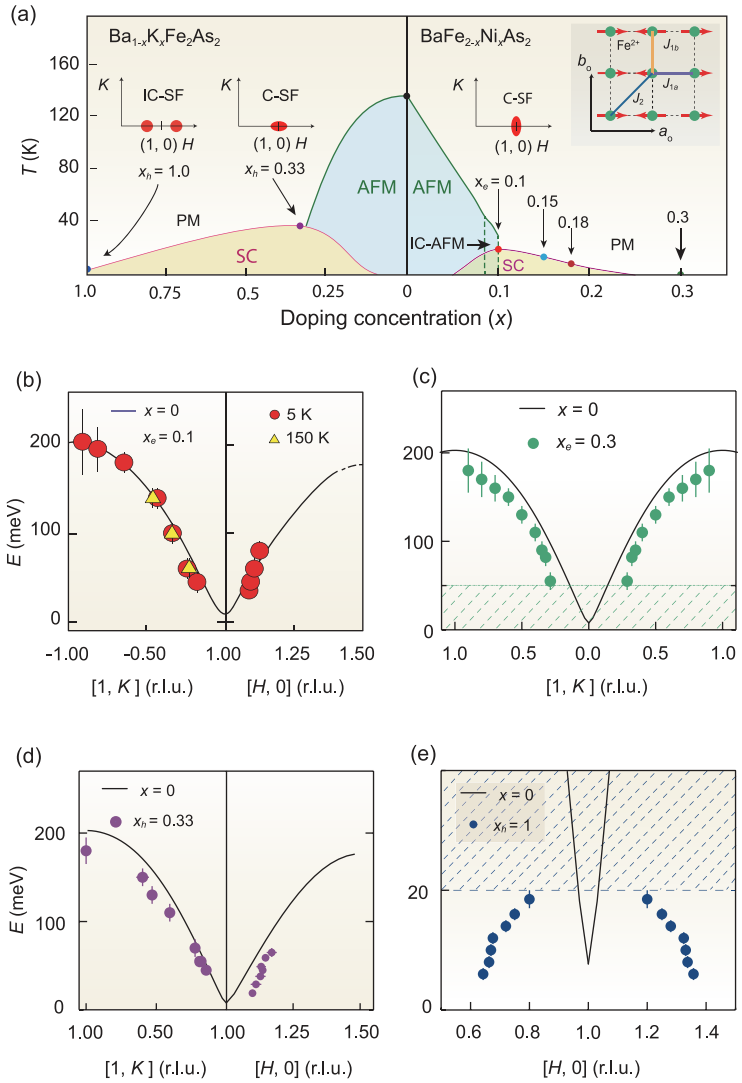

Figure 5. (a) The electronic phase diagram of electron and hole-doped $BaFe_2As_2$, where the arrows indicate the doping levels of INS experiments. The right inset shows crystal and AF spin structures of $BaFe_2As_2$ with marked the nearest (J_{1a}, J_{1b}) and next-nearest neighbor (J_2) magnetic exchange couplings. The inset above $x_e = 0.1$ shows the transversely elongated ellipse representing the low-energy spin excitations in electron-doped $BaFe_{2-x}Ni_xAs_2$ in the (*H*, *K*) plane of the reciprocal space. The left insets show the evolution of low-energy spin excitations in hole-doped $Ba_{1-x}K_xFe_2As_2$ in the (*H*, *K*) plane. C-SF and IC-SF indicate commensurate and incommensurate spin fluctuations, respectively. (b)–(e) The solid lines in the figure are spin wave dispersions of the undoped $BaFe_2As_2$ along the two high-symmetry directions. The symbols in (b), (c), (d), and (e) are dispersions of spin excitations for $BaFe_{1.9}Ni_{0.1}As_2$, $BaFe_{1.7}Ni_{0.3}As_2$, $Ba_{0.67}K_{0.33}Fe_2As_2$, and KFe_2As_2, respectively [83]. The shaded areas indicate vanishing spin excitations.

FeP, FeAs, FeSe to FeTe. Due to the relative small h in FeP-based superconductors, their T_cs are usually lower than those in FeAs-based superconductors. For example, in La-1111 phase, as P is substituted by As, T_c is enhanced dramatically from 7 to 26 K, due to the increase in h. For FeAs-based 1111 phase, as the substitutions of La by Nd and Sm increase h to around 1.38 Å, T_c increases dramatically from 26 to 56 K. After crossing this maximum, the T_c of $TbFeAsO_{0.7}$, $Ba_{0.6}K_{0.4}Fe_2As_2$, NaFeAs or LiFeAs decreases with increasing h. The data of optimally doped $FeSe_{1-x}Te_x$, $FeSe_{0.57}Te_{0.43}$, seem to also follow the same curve. As a result, such a dependence of T_c on h seems to be universal for 1111, 122, 111, and 11 iron-based superconductors. Though the maximum T_c of the superconductors with thick blocking layer remains unconfirmed, the data of the 42622 superconductor obey the same universal curve, except for a small deviation, which may suggest that the enhancement of 2D character could induce a T_c higher than 56 K. It should be noted that for such a universal correspondence between h and T_c, there is an exception in FeSe-derived superconductors. As shown in Fig. 4b, for the FeSe-derived materials, a minimum of T_c can be observed at $h \approx 1.45$ Å [36], instead of a maximum as shown in Fig. 4a. This may suggest some new underlying physics in FeSe-derived superconductors compared to FeAs-based ones. The bond angle of As-Fe-As, which reflects the distortion of the $FeAs_4$ tetrahedron, was also thought to be closely related to superconductivity [66]. As shown in Fig. 4c, the maximum T_c was achieved when the $FeAs_4$ tetrahedron is perfectly regular, with the bond angle of 109.47°.

THE INTERPLAY BETWEEN MAGNETISM AND SUPERCONDUCTIVITY

Soon after the discovery of iron pnictide superconductor $LaFeAsO_{1-x}F_x$ with $T_c = 26$ K [3], band calculations based on transport and optical conductivity measurements predicted the presence of a collinear antiferromagnetic (CAF) [or spin-density-wave (SDW)] state in the parent compounds [67], which was subsequently confirmed by neutron scattering experiments as shown in the inset of Fig. 5 [58]. The same CAF state was later found in the parent compounds of most iron pnictide superconductors [62]. Although the electronic phase diagrams for different families of iron-based superconductors can be somewhat different [21], they all share the common feature of an AF ordered parent compound [68]. This has inspired many to believe that the magnetic excitations play an important role in the mechanism of the high-T_c superconductivity in iron-based superconductors [69]. To test if this is indeed the case, systematic investigation on the magnetic order and spin excitations throughout the phase diagram of different families of iron-based superconductors is essential. Fig. 5 shows the electronic phase diagram of electron- and hole-doped $BaFe_2As_2$ iron pnictides determined from transport and neutron scattering experiments [24,70–77]. For electron-doped

$BaFe_{2-x}Ni_xAs_2$, the maximum $T_c = 20$ K is around $x \approx 0.1$ and superconductivity ceases to exist for $x \geq 0.25$ [78]. For hole-doped $Ba_{1-x}K_xFe_2As_2$, superconductivity exists in the entire phase diagram with maximum $T_c = 38$ K near $x \approx 0.33$ and $T_c = 2$ K for pure KFe_2As_2 [79]. The arrows in the figure indicate iron pnictides where spin excitations in the entire Brillouin zone have been mapped out by inelastic neutron scattering (INS) experiments [80–86].

Effect of electron doping on spin waves of iron pnictides

We first discuss the electron-doping evolution of spin excitations in $BaFe_{2-x}Ni_xAs_2$. With the development of neutron time-of-flight spectroscopy, the entire spin wave spectra were obtained in $CaFe_2As_2$ [87] and $BaFe_2As_2$ [80] soon after the availability of single crystals of these materials. The solid lines in Fig. 5b show the dispersion of spin waves in $BaFe_2As_2$ along the $[1, K]$ and $[H, 0]$ directions in reciprocal space, where the CAF order occurs at the $Q_{AF} = (1, 0)$ wave vector position [80]. Upon electron doping to induce optimal superconductivity, spin excitations become broader at low energies ($E \leq 80$ meV) while remain unchanged at high energies ($E > 80$ meV) [81]. The low-energy spin excitations couple to superconductivity via a collective spin excitation mode termed neutron spin resonance [88–91], seen also in copper oxide superconductors [92]. The red circle and yellow upper triangle symbols in Fig. 5b show spin excitation dispersions of the optimally electron-doped $BaFe_{1.9}Ni_{0.1}As_2$ at $T = 5$ and 150 K, respectively [81]. With further electron doping, superconductivity is suppressed for $x \geq 0.25$ [78], Fig. 5c shows the dispersions of spin excitations of $BaFe_{1.7}Ni_{0.3}As_2$ compared with that of the undoped $BaFe_2As_2$ [80,83]. A large spin gap forms for energies below ~50 meV, as shown in the dashed line region. The dispersions of spin excitations are also softer than that of $BaFe_2As_2$ [80,83]. Fig. 5d and e shows the dispersions of spin excitations for optimally hole-doped $Ba_{0.67}K_{0.33}Fe_2As_2$ and hole-overdoped KFe_2As_2, respectively. The solid lines are the spin wave dispersions of $BaFe_2As_2$ [80,83].

Fig. 6 summarizes the evolution of the 2D constant-energy images of spin excitations in the (H, K) plane at different energies as a function of electron doping from the undoped AF parent compound $BaFe_2As_2$ to overdoped non-SC $BaFe_{1.7}Ni_{0.3}As_2$ [75,80,83]. In the undoped case, there is an anisotropy spin gap below ~15 meV so there is essentially no signal at $E = 9 \pm 3$ meV (Fig. 6a). Upon electron doping to suppress static AF order and induce near-optimal superconductivity with $x = x_e = 0.096$, the spin gap is suppressed and low-energy spin excitations are dominated by a resonance that couples with superconductivity (Fig. 6f) [75,89–91]. Moving to electron-overdoped side with reduced superconductivity in $BaFe_{2-x}Ni_xAs_2$ with $x = 0.15$ ($T_c = 14$ K) and 0.18 ($T_c = 8$ K), spin excitations at $E = 8 \pm 1$ meV become weaker and more transversely elongated (Fig. 6k and p) [75]. Finally on increasing the electron-doping level to $x = 0.3$ with no superconductivity, a large spin gap forms in the low-energy excitation spectra (Fig. 6u). Fig. 6b–6e, 6g–6j, 6i–6o, 6q–6t, and 6v–y shows spin excitations at different energies for $BaFe_{2-x}Ni_xAs_2$ with $x = 0$, 0.096, 0.15, 0.18, and 0.30, respectively. While spin excitations at energies below $E = 96 \pm 10$ meV change rather dramatically with increasing electron doping, high-energy spin excitations remain similar and only soften slightly.

The effect of hole doping on the spin excitations of iron pnictides

Fig. 7 shows the evolution of spin excitations in the similar 2D constant-energy images as a function of hole doping. For pure KFe_2As_2, incommensurate spin excitations along the longitudinal direction are seen at $E = 8 \pm 3$ meV (Fig. 7a) and 13 ± 3 meV (Fig. 7b) [86]. Upon further increasing energy, no clear magnetic scattering can be seen (Fig. 7c). For optimally hole-doped $Ba_{0.67}K_{0.33}Fe_2As_2$, the low-energy spin excitations change from transversely elongated ellipses as shown in Fig. 6f to longitudinally elongated ellipse at $E = 5 \pm 1$ meV (Fig. 7d). On increasing the energy to the neutron spin resonance energy of $E = 15 \pm 1$ meV, spin excitations become isotropic in reciprocal space (Fig. 7e). Spin excitations become transversely elongated again for energies above $E = 50 \pm 2$ meV (Fig. 7f–i), very similar to spin excitations in electron-doped $BaFe_{2-x}Ni_xAs_2$ (Fig. 6). From data presented in Figs 6 and 7, one can establish the basic trend in the evolution of spin excitations via electron and hole doping to the parent compound $BaFe_2As_2$. While electron doping appears to mostly modify the low-energy spin excitations and make them more transversely elongated with increasing electron counts, high-energy spin excitations do not change dramatically. Therefore, the Fermi surface modifications due to electron doping affect mostly the low-energy spin excitations, suggesting that they are arising from itinerant electrons. The high-energy spin excitations weakly dependent on electron-doping-induced Fermi surface changes are most likely arising from localized moment. The lineshape change

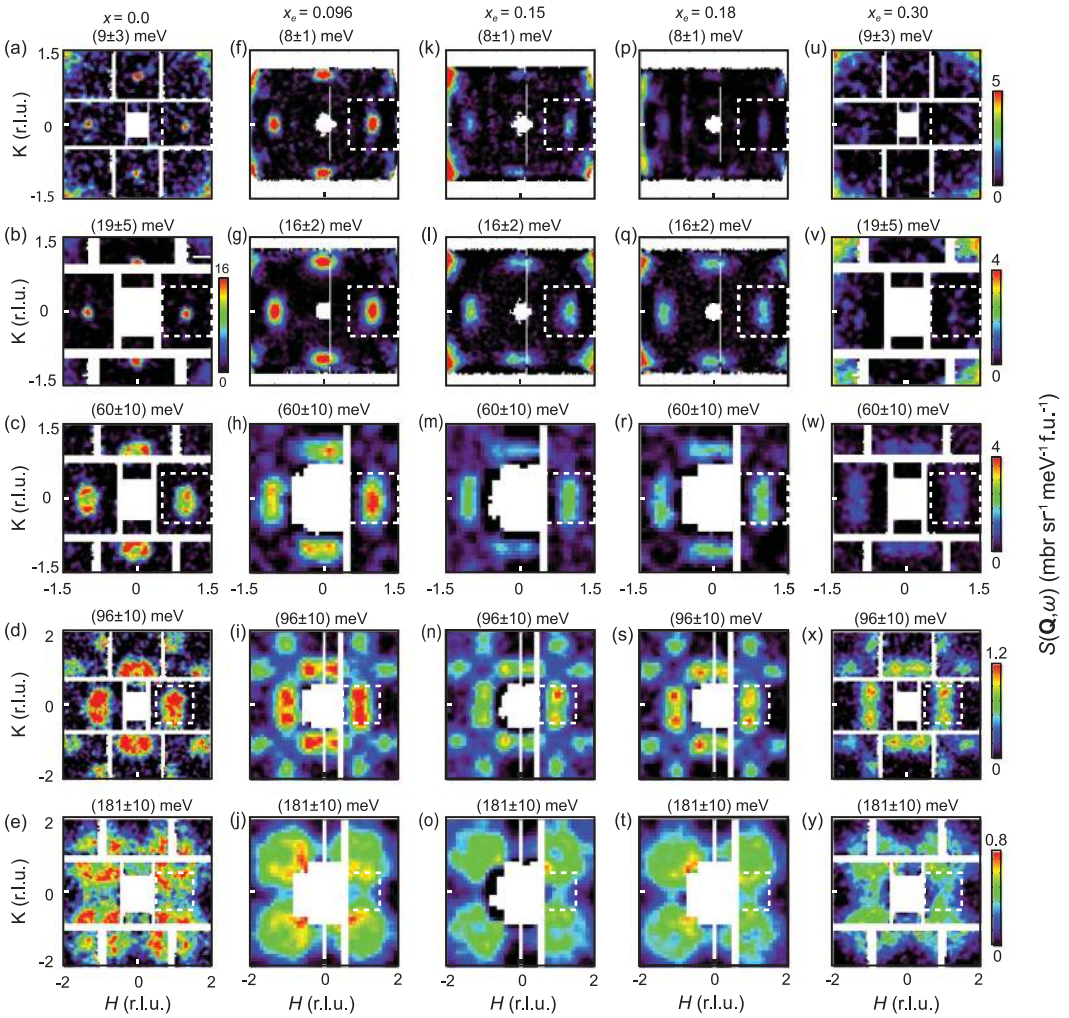

Figure 6. Constant-energy slices through magnetic excitations of electron-doped iron pnictides at different energies. The color bars represent the vanadium normalized absolute spin excitation intensity in the units of mbarn sr^{-1} meV^{-1} f.u.$^{-1}$. (a)–(e) Spin waves of $BaFe_2As_2$ at excitation energies of $E = 9 \pm 3$, 19 ± 5, 60 ± 10, 96 ± 10, and 180 ± 10 meV [80]. Spin waves peak at the AF ordering wave vectors $Q_{AF} = (\pm 1, 0)$ in the orthorhombic notation. Spin waves are also seen at $Q_{AF} \approx (0, \pm 1)$ due to the twin domains of the orthorhombic structure. (f)–(j) 2D images of spin excitations for $BaFe_{1.904}Ni_{0.096}As_2$ at $E = 8 \pm 1$, 16 ± 2, 60 ± 10, 96 ± 10, and 181 ± 10 meV. Identical slices as that of (f)–(j) for (k)–(o) $BaFe_{1.85}Ni_{0.15}As_2$ and (p)–(t) $BaFe_{1.82}Ni_{0.18}As_2$ [75]. (u)–(y) Constant-energy slices through magnetic excitations of electron-overdoped doped non-SC $BaFe_{1.7}Ni_{0.3}As_2$ at $E = 9 \pm 3$, 19 ± 5, 60 ± 10, 96 ± 10, and 181 ± 10 meV [83].

from transversely to longitudinally elongated ellipse in low-energy spin excitations of iron pnictides upon hole doping is consistent with the random phase approximation calculation of the doping dependence of the nested hole and electron Fermi surfaces [84,93]. The absence of dramatic changes in high-energy spin excitations again suggests the presence of local moments independent of Fermi surface changes induced by electron or hole doping. Comparing with resonant inelastic X-ray scattering (RIXS) results on hole-doped $Ba_{0.6}K_{0.4}Fe_2As_2$ [94], we note that dispersion determined from RIXS is consistent with neutron scattering while the intensity is lower. At present, it is unclear how to understand the intensity of the RIXS measurements.

Evolution of local dynamic susceptibility as a function of electron and hole doping

To quantitatively determine the electron- and hole-doping evolution of the spin excitations in iron pnictides, one can estimate the energy dependence of the local dynamic susceptibility per formula unit, defined as $\chi''(\omega) = \int \chi''(\mathbf{q}, \omega) d\mathbf{q} / \int d\mathbf{q}$, where $\chi''(\mathbf{q}, \omega) = (1/3) tr(\chi''_{\alpha\beta}(\mathbf{q}, \omega))$ [81,95]. The dashed squares in Figs 6 and 7 show the integration region of the local dynamic susceptibility in reciprocal space. Fig. 8a and b summarizes the energy dependence of the local dynamic susceptibility for hole ($Ba_{1-x_h}K_{x_h}Fe_2As_2$ with $x_h = 0$, 0.33, 1) and electron ($BaFe_{2-x_e}Ni_{x_e}As_2$ with $x_e = 0$, 0.096,

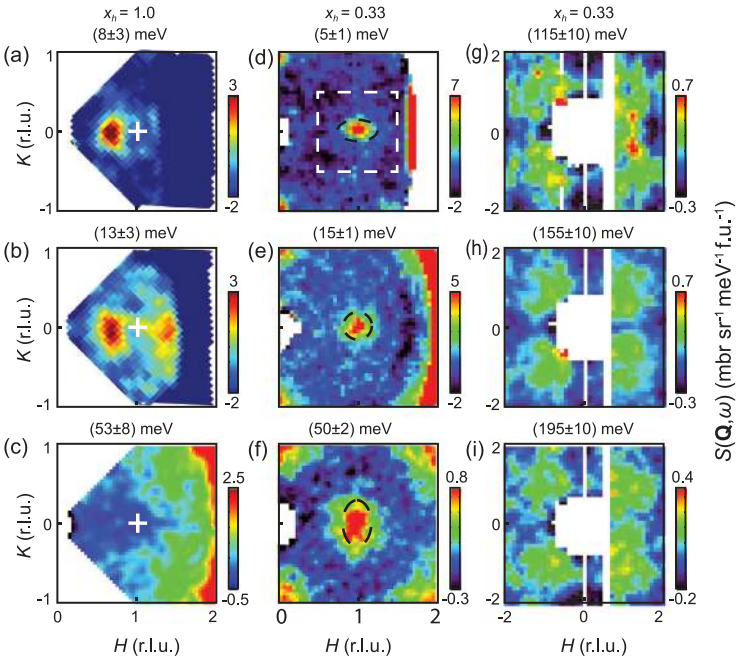

Figure 7. 2D images of spin excitations at different energies for hole-doped KFe_2As_2 at 5 K. (a) $E = 8 \pm 3$ meV obtained with $E_i = 20$ meV along the *c*-axis. The right side incommensurate peak is obscured by background scattering. (b) 13 ± 3 meV with $E_i = 35$ meV, and (c) 53 ± 8 meV with $E_i = 80$ meV. For $Ba_{0.67}K_{0.33}Fe_2As_2$ at $T = 45$ K, images of spin excitations at (d) $E = 5 \pm 1$ meV obtained with $E_i = 20$ meV, (e) 15 ± 1 meV with $E_i = 35$ meV, and (f) 50 ± 2 meV obtained with $E_i = 80$ meV. Spin excitations of $Ba_{0.67}K_{0.33}Fe_2As_2$ at energy transfers (g) 115 ± 10 meV; (h) 155 ± 10 meV, (i) 195 ± 10 meV obtained with $E_i = 450$ meV, all at 9 K. Wave vector-dependent backgrounds have been subtracted from the images [83].

0.15, 0.18, 0.3) doped iron pnictides. From Fig. 8a, we see that the effect of hole-doping near-optimal superconductivity is to suppress high-energy spin excitations and transfer spectral weight to lower energies. The intensity changes across T_c for hole-doped $Ba_{0.67}K_{0.33}Fe_2As_2$ are much larger than that of the electron-doped $BaFe_{1.9}Ni_{0.1}As_2$ [81]. As a function of increasing electron doping, the local dynamic susceptibility at low energies decreases and finally vanishes for electron-overdoped non-SC $BaFe_{1.7}Ni_{0.3}As_2$ with no hole-like Fermi surface [75,83]. This again confirms the notion that superconductivity in iron pnictide is associated with itinerant electron and low-energy spin excitation coupling between the nested hole and electron Fermi surfaces [83].

Correlation between spin excitations and superconductivity

In conventional BCS superconductors [96], superconductivity occurs via electron–lattice coupling below T_c. The SC condensation energy E_c $(= -N(0)\Delta^2/2$ and $\Delta \approx 2\hbar\omega_D e^{-1/N(0)V_0}$, where $N(0)$ is the electron density of states at zero temperature) and T_c are controlled by the strength of the Debye energy $\hbar\omega_D$ and electron–lattice coupling V_0 [96–98]. For unconventional superconductors derived from electron and hole doping to their AF ordered parent compounds, short-range spin excitations may mediate electron pairing for superconductivity [69]. Here, the SC condensation energy should be accounted for by the change in magnetic exchange energy between the normal (N) and superconducting (S) phases at zero temperature via $\Delta E_{ex}(T) = 2J[\langle \mathbf{S}_{i+x} \cdot \mathbf{S}_i \rangle_N - \langle \mathbf{S}_{i+x} \cdot \mathbf{S}_i \rangle_S]$, where J is the nearest neighbor magnetic exchange coupling, $\langle \mathbf{S}_{i+x} \cdot \mathbf{S}_i \rangle$ is the dynamic spin susceptibility in absolute units at temperature T, and $S(\mathbf{Q}, E = \hbar\omega)$ is related to the imaginary part of the dynamic susceptibility $\chi''(\mathbf{Q}, \omega)$ via $S(\mathbf{Q}, \omega) = [1 + n(\omega, T)]\chi''(\mathbf{Q}, \omega)$ with $[1 + n(\omega, T)]$ being the Bose population factor [69].

Since the dominant magnetic exchange couplings are isotropic nearest neighbor exchanges for copper oxide superconductors [99,100], the magnetic exchange energy $\Delta E_{ex}(T)$ can be directly estimated using the formula through carefully measuring of J and the dynamic spin susceptibility in absolute units between the normal and SC states [101–103]. For heavy Fermion [104] and iron pnictide superconductors [83], one has to modify the formula to include both the nearest neighbor and next-nearest neighbor magnetic exchange couplings. The calculations of the magnetic exchange energies in $CeCu_2Si_2$ [104] and optimally hole-doped $Ba_{0.67}K_{0.33}Fe_2As_2$ [83] reveal that they are large enough to account for the SC condensation energy, thus suggesting that spin excitations could be the driving force for mediating electron pairing for superconductivity. These results are consistent with NMR experiments [105], where the presence of low-energy spin excitations is found to be associated with Fermi surface nesting and the absence of nesting in electron-overdoped iron pnictides suppresses the low-energy spin excitations. These results are also consistent with the absence of spin excitations in non-SC collapsed tetragonal (cT) phase of $CaFe_2As_2$ from INS measurements [106].

ELECTRONIC PROPERTIES

Electronic properties of the iron-based superconductors are critical for understanding their phase diagram, mechanism, and transport behaviors. In this section, we focus on the electronic properties of these compounds obtained by ARPES, in link with some results from scanning tunneling microscopy/spectroscopy (STM/STS)

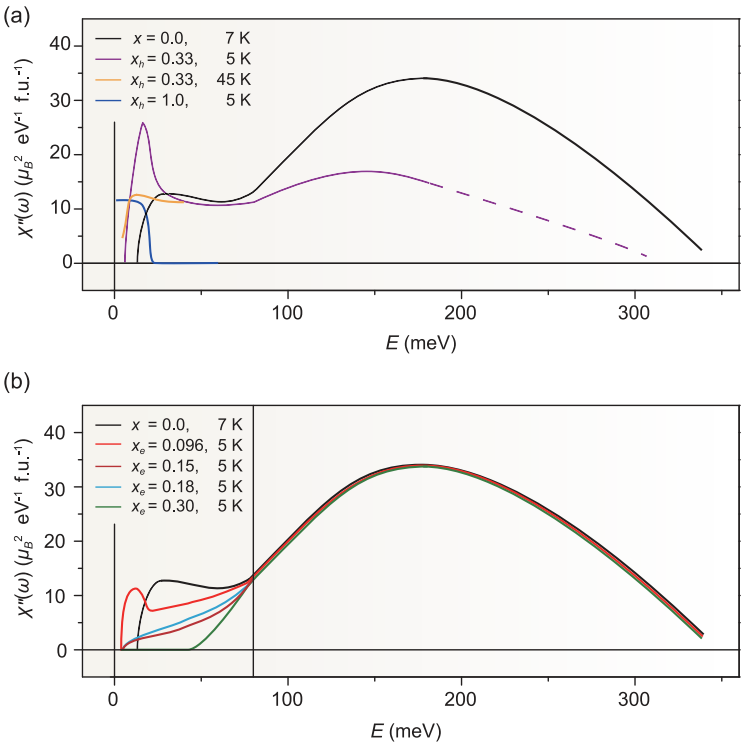

Figure 8. Energy and temperature dependence of the local dynamic susceptibility $\chi''(\omega)$ for (a) $BaFe_2As_2$, $Ba_{0.67}K_{0.33}Fe_2As_2$, KFe_2As_2, and (b) $BaFe_{2-x_e}Ni_{x_e}As_2$ with $x_e = 0$, 0.096, 0.15, 0.18, 0.3. The intensity is in absolute unit of μ_B^2 eV^{-1} f.u.$^{-1}$ obtained by integrating the $\chi''(Q, \omega)$ in the dashed regions specified in Figs 6 and 7.

measurements. We note that more detailed reviews of the ARPES results can be found in [212,213].

The electronic structure of the iron-based superconductors and related materials is characterized by the multi-band and multi-orbital nature [107]. Based on their Fermi surface topology, one could generally divide them into two categories: (1) systems with both electron and hole Fermi surfaces, and (2) systems with only electron Fermi surfaces. Most of the iron pnictides and Fe(Te, Se) bulk materials belong to the first category [108–112], while $A_xFe_{2-y}Se_2$, single-layer FeSe on STO, and heavily electron-doped iron pnictides belong to the second category [113–116]. Since most of the iron-based superconductors are in the first category, we will discuss its electronic properties in the following first three subsections, while those of the second category will be discussed in the fourth subsection. In the last subsection, we will discuss the role of correlations and some overall understandings of the electronic structure.

Basic electronic structure

The low-energy electronic structure of iron-based superconductors is dominated by the Fe 3d states [117]. The unit cell contains two Fe ions, because there are pnictogen and chalcogen ions above and below the iron plane. As a result, there would be totally ten 3d states and thus ten bands. However, it was found both by polarization-dependent ARPES experiments and density functional theory (DFT) calculations that the Fermi surface is usually composed of three hole-like Fermi surfaces near the zone center and two electron Fermi surfaces around the zone corner. The d_{xy}, d_{xz}, and d_{yz} orbitals are the main contributor to the states near the Fermi energy E_F [118,119]. Fig. 9a illustrates a typical band structure along the Γ–M direction, and Fig. 9b shows the measured Fermi surface of $BaFe_2(As_{0.7}P_{0.3})_2$ in its 3D Brillouin zone [120]. The Fermi surface topology and band structure are rather similar for the 11, 111, 122, and 1111 series of iron-based superconductors [108–112].

Strictly speaking, the iron-based superconductors are 3D materials; however, the electron hopping along the c direction is not strong, so that the warping of the Fermi surface along the k_z direction is not so obvious for most of the bands. However, the α band shows strong k_z dependence, and its Fermi surface exhibits large warping in Fig. 9b.

The carrier density of iron-based superconductors can be tuned by doping in the charge reservoir layer or at the Fe site. Electron and hole doping can be varied over a large range, which in turn varies the chemical potential and the Fermi surface. Fig. 9c shows the hole-doping evolution of the Fermi surface sheets in $Ba_{1-x}K_xFe_2As_2$ and the electron-doping evolution of the Fermi surface sheets in $NaFe_{1-x}Co_xAs$. With sufficient doping, Lifshitz transitions of the Fermi surface topology eventually occur in both cases [116,121].

In the case of isovalent doping, such as Ru for Fe, P for As, or Te for Se, the Fermi surface volume usually does not change, or change slightly for some unknown reason, but the individual Fermi surface sheets may change noticeably by the induced chemical pressure [120,122]. The band renormalization factor also generally decreases with doping, which indicates the weakened correlation.

Compared with the cuprate superconductors, which are doped Mott insulators, the iron-based superconductors are less sensitive to impurities. However, the large amount of dopants will cause serious scattering of the quasi-particles that needs to be taken into account in understanding the transport and SC properties. The d_{xy}-based γ band near the zone center is somehow more sensitive to impurities [116]. The impurity scattering also strongly depends on the locations of the dopants, which in the increasing order is off-plane, at the pnictogen/chalcogen site and at the iron site [116,123].

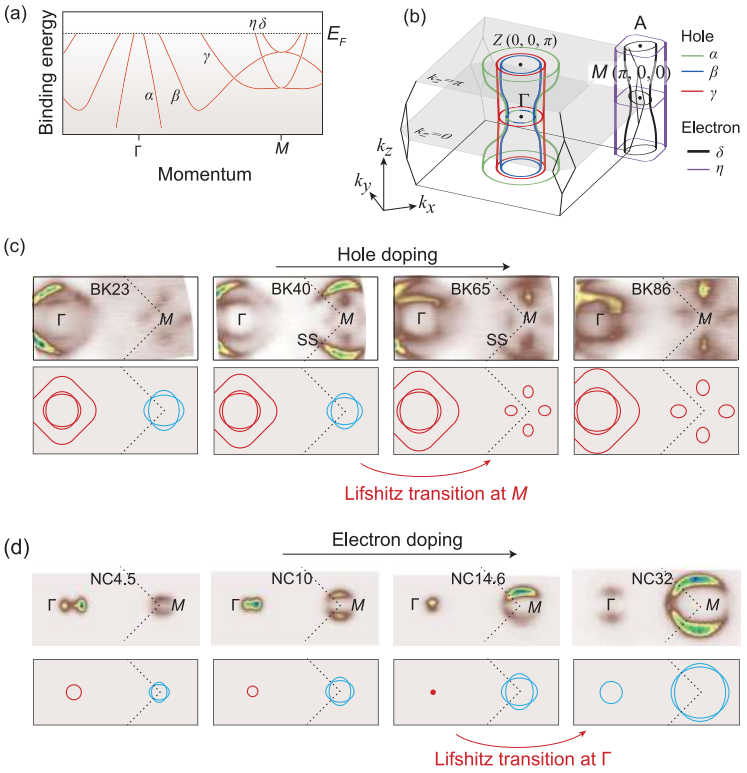

Figure 9. (a) Cartoon of the band structure in iron pnictides. (b) The typical 3D Fermi surface of iron pnictides $BaFe_2(As_{0.7}P_{0.3})_2$ [124]. (c) The doping dependence of Fermi surface topology taken in $Ba_{1-x}K_xFe_2As_2$. The upper panels show the photoemission intensity distribution at E_F. The lower panels show the obtained Fermi surface. SS is the abbreviation of surface state. The red and blue lines illustrate the hole pockets and electron pockets, respectively. (d) is the same as panel (c), but taken in $NaFe_{1-x}Co_xAs$.

The nematic phases

The nematic phases here refer to the CAF state and the orthorhombic phase below the structural transition temperature T_s, as illustrated in Fig. 10a [125]. There are signs of a ferromagnetic orbital ordered phase above T_s, which exhibits nematicity as well [126,127]. Such a nematicity can be viewed in the resistivity of detwinned sample shown in Fig. 10b. STM has found nematic order with large periods, which has not been observed by bulk measurements [128].

In the beginning, the nesting between the electron and hole Fermi surface sheets was considered to be the driving force of the CAF state, as it coincides with the $(\pi, 0)$ ordering wave vector [67]. As a result, sometimes the CAF state was called SDW. However, it was soon found that a good nesting often does not correspond to a CAF state [116]. On the other hand, when the hybridization gap occurs, it is well below E_F due to crossing with the folded bands. Moreover, the entire bands shifts, instead of just in the vicinity of the crossing [108,110].

The evolution of the nematic electronic structure is illustrated with the example of NaFeAs, where the T_s is above the Neel temperature [129]. The sample was detwinned with moderate pressure, so that the electronic structure along different directions is disentangled, starting from a slightly higher temperature T_s' than T_s. As shown in Fig. 10c, the Γ–M_x and Γ–M_y are not equivalent in the nematic phases. The electronic structure behaves drastically differently in these two directions (Fig. 10d and e in the nematic phases). For the β band whose dispersions are the same along these two directions in the tetragonal paramagnetic (PM) phase, its position starts to move in different directions below T_s', which is clearly demonstrated by Fig. 10f–h. The band position difference (Δ_{H0}) saturates at low temperatures eventually. Similar behavior has been observed in detwinned $BaFe_{2-x}Co_xAs_2$ (Fig. 10i) as well, showing that it generally occurs in different compounds [130]. Such a smooth temperature evolution across both the structural and magnetic transitions indicates that they are of the same origin, and the nematic phases are characterized by the same electronic structure nematicity [110]. Different phases could be viewed as different stages of the same evolution. At high temperatures, although the structure is tetragonal, the electronic nematicity already occurs above T_s, and the hopping parameters along a and b start to differ. As a result, the occupations of d_{xz} and d_{yz} orbitals become inequivalent at all Fe sites, which can be viewed as an ferromagnetic orbital order [127], although such a difference could be rather small, just a few percent in the NaFeAs case down to the lowest temperature [129]. Short-ranged or fluctuating CAF order might have occurred, in association with the nematicity. It was suggested that the spin order is more 2D and more susceptible to fluctuations, so that the Neel temperature is lower than T_s in some cases [131]. The electronic (spin, charge, orbital) and structural degrees of freedom all participate into this process, so that it is likely difficult and unnecessary to identify which is the dominating driving force. Nevertheless, the total electronic energy is reduced significantly, which is well beyond the energy due to the structural change.

The anisotropy of the resistivity in the nematic phase is consistent with the anisotropic electronic structure; however, recent STM measurements showed that the impurity scattering can be rather anisotropic [128]. This explains the variations of the resistivity anisotropy in different compounds. Further investigations are needed to clarify this issue.

FeTe is a special parent compound of iron-based superconductors, which exhibits a bicollinear AF order [132,133]. Its polaronic electronic structure is rather different from those of iron pnictides, which is consistent with its large local moment though

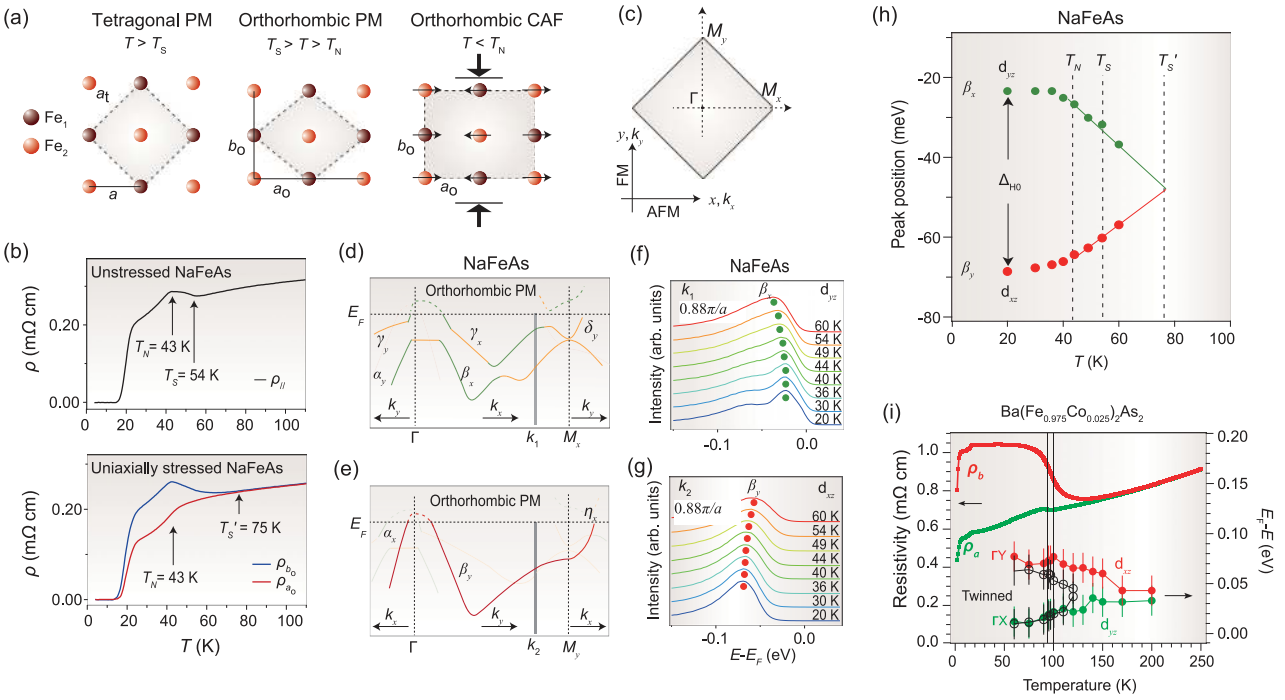

Figure 10. (a) Cartoon of the lattice and spin structure in tetragonal PM, orthorhombic PM, and orthorhombic CAF state for iron pnictides. The large black arrows show the direction of the uniaxial pressure applied in the mechanical detwinning process. (b) The temperature-dependent resistivity of unstressed and uniaxially stressed NaFeAs, respectively. (c) The definition of the projected 2D Brillouin zone for NaFeAs. The *x* and *y* axes are defined along the iron–iron directions. (d) The band structure in the orthorhombic PM state along Γ–M_x and some other high-symmetry directions, where only d_{yz}- and d_{xy}-dominated bands are highlighted. (e) is the same as panel (d), but mainly along the Γ–M_y direction, with the d_{xz}-dominated bands highlighted. (f) and (g) The temperature dependence of the EDCs at k_1 and k_2, as indicated by the gray line in panels (d) and (e), respectively. (h) The peak positions of the β_x and β_y bands as functions of temperature. The maximal observable separation between β_x and β_y at the same momentum value (i.e. $|k_x| = |k_y|$) near M_x and M_y, respectively, is defined as Δ_H. Δ_H is a function of temperature, and its low-temperature saturated value is defined as Δ_{H0}. (i) Energy position of the d_{xz} and d_{yz} bands as a function of temperature, measured on both detwinned and unstressed $Ba(Fe_{0.975}Co_{0.025})_2As_2$, compared with resistivity measurements [125]. Data are taken from [129,130].

[111,134]. The magnetic order in FeTe can be explained by the exchange interactions amongst local moments as well.

The SC phase

There are two critical issues in the electronic structure of the SC state: (1) what is the pairing symmetry, and (2) what determines the T_c.

Pairing symmetry is manifested in the SC gap distribution. For conventional phonon-mediated s-wave superconductors, the gap is nodeless, i.e. the Fermi surface is fully gapped. While for cuprates, there are nodes (zero gap) along the diagonal directions, reflecting its d-wave symmetry. However, for iron-based superconductors, there are both nodal and nodeless members [135–144].

Nodeless SC gap

A large fraction of the iron pnictides are nodeless based on thermal conductivity, penetration depth, STS, and other measurements [145–148]. For such a multi-band system, the gap amplitudes vary on different Fermi surface sheets [149]. On individual Fermi surface sheets, the in-plane gap distribution is often isotropic (within the experimental uncertainty), e.g. for $Ba_{1-x}K_xFe_2As_2$ shown in Fig. 11a. The anisotropy along the k_z direction usually is negligible for most Fermi pockets, but some noticeable dependence was found for the α Fermi surface with a sizable warping, as shown in Fig. 11b. For some compounds, such as LiFeAs and Fe(Te,Se), the in-plane gap distribution could be anisotropic as plotted in Fig. 11e , which was attributed to the Fermi surface shape or different pairing interactions mediated by various exchange interaction terms.

Theoretically, the $s^{\pm}$-wave pairing symmetry was proposed for the iron-based superconductors [150,151]. However, its proof requires phase-sensitive techniques to detect the phase difference among various Fermi surface sheets. The magnetic field dependence of the quasi-particle interference pattern of Fe(Te, Se) observed by STM was shown to support the $s^{\pm}$-wave phase-changing scenario [152].

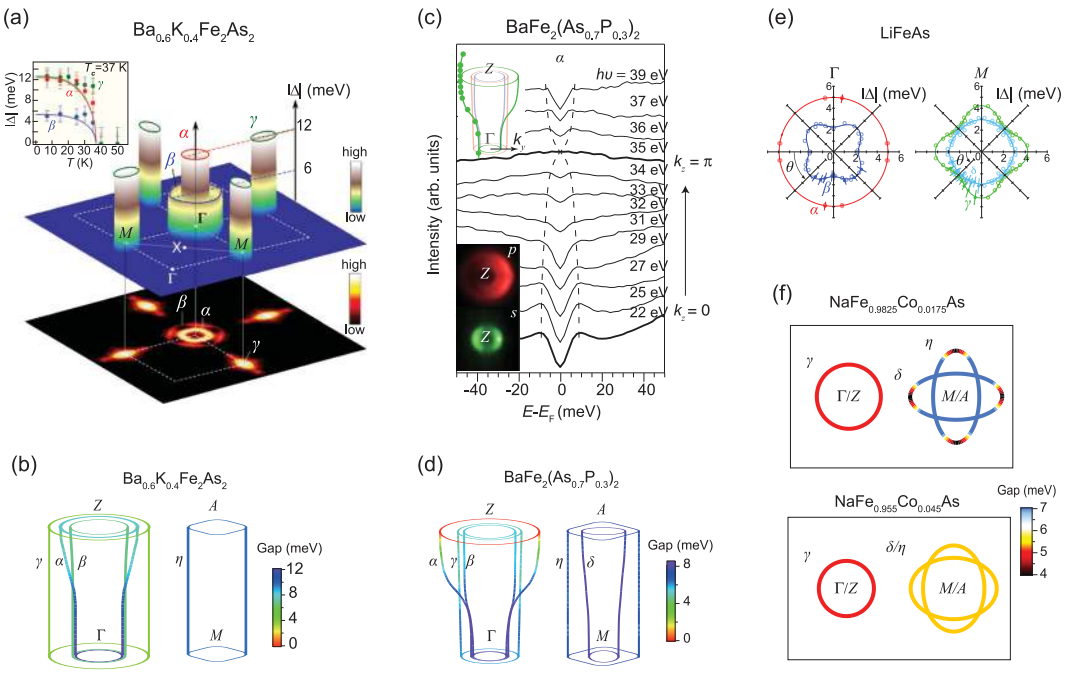

Figure 11. (a) The illustration of the in-plane gap distribution on the Fermi surface in $Ba_{0.6}K_{0.4}Fe_2As_2$. The inset shows the temperature dependence of the SC gap. (b) Illustration of the gap distribution on the 3D Fermi surface in $Ba_{0.6}K_{0.4}Fe_2As_2$. (c) k_z dependence of the symmetrized spectra measured on the α hole Fermi surface in $BaFe_2(As_{0.7}P_{0.3})_2$. The dashed line is a guide to the eyes for the variation of the SC gap at different k_z values. The inset shows the polarization-dependent Fermi surface maps around Z, indicating the α pocket around Z is mainly composed of the d_z^2 orbital. (d) Illustration of the gap distribution on the 3D Fermi surface of $BaFe_2(As_{0.7}P_{0.3})_2$. (e) and (f) The in-plane SC gap distribution on LiFeAs and $NaFe_{1-x}Co_xAs$, respectively. Data are taken from [124,135,159,214].

Nodal SC gap

The nodal SC gap was found in some iron pnictides with pnictogen height less than 1.33 Å, KFe_2As_2, and FeSe film grown on graphene [141,143,144]. As shown in Fig. 11c–d, the nodal gap of $BaFe_2(As_{1-x}P_x)_2$ is located in a ring around Z on the α hole pocket with significant warping and contribution from the d_{z^2} orbital [124]. This indicates its 'accidental' appearance, and rules out the symmetry-related origin of the nodes [150,151]. Theoretically, it has been shown that d_{z^2} does not contribute much to pairing [153]. This hole Fermi pocket is from the same α band whose gap shows significant k_z dependence in the optimally doped $Ba_{1-x}K_xFe_2As_2$ (Fig. 11b); thus, similar origin is expected for both.

For KFe_2As_2 and heavily doped $Ba_{1-x}K_xFe_2As_2$, laser-ARPES work indicates that the gap nodes appear at certain points around Z on a Fermi pocket with strong d_{z^2} characters [154], while some other ARPES studies show that they appear on some small hole pockets near M as vertical nodal lines [155]. Whether these are due to sample dependence or due to the high k_z resolution of laser-ARPES needs further clarification. However, the important message is that the nodes in these compounds are accidental, and not due to d-wave or other phase-changing pairing symmetry. This unites the nodal and nodeless gap behavior in one single scheme.

Gap in CAF/superconductivity coexisting regime

As demonstrated by μSR, neutron scattering and ARPES studies, there is a unique SC regime in the phase diagram of iron-based superconductors, where CAF order and superconductivity coexist [156–160]. Particularly, the recent STM measurements of $NaFe_{1-x}Co_xAs$ show the microscopic coexistence and competition of these two orders [161]. The presence of such a unique regime puts strong constraints on the possible paring symmetry. For example, such a coexistence would not be possible, had the pairing symmetry been s^{++}-wave type, where the phases of the SC order parameter are the same on various Fermi surface sheets. On the other hand, some calculations based on the $s^{\pm}$-wave pairing suggest that CAF order would induce strong gap anisotropy, and by increasing strength of the CAF order, even nodes could be induced [162,163]. Consistently, a strong gap anisotropy has been observed

on the electron Fermi surfaces for $NaFe_{1-x}Co_xAs$ in the coexisting regime, but not in the pure SC regime (Fig. 11f), although their dopings differ just slightly.

This might explain the nodal gap observed in the FeSe film grown on a graphene substrate by STS, since obvious signs of CAF order or strong fluctuations have been observed by the recent ARPES measurements of multi-layer FeSe films grown on the STO substrate [115,144]. As a comparison, the STS measurements show that the gap of Fe(Te, Se) is nodeless, where CAF order is not present [152].

Electronic features correlated or uncorrelated with the superconductivity

T_c-determining factors are crucial for understanding the mechanism of superconductivity in unconventional superconductors. Many empirical observations have been made as to what affects the T_c for iron-based superconductors. First of all, it was found that near the optimal doping of some iron pnictides, certain electron and hole Fermi pockets are better nested, namely they can overlap on each other when shifted [136]. While doped away from the optimal doping, the nesting worsens, since electron and hole pockets change differently. However, various counter examples have been found later.

In some iron pnictides, such as $BaFe_{2-x}Co_xAs_2$ and $NaFe_{1-x}Co_xAs$, it was found that the superconductivity diminishes when the system is doped with sufficient electrons so that a Lifshitz transition occurs (specifically, the d_{xz}/d_{yz}-based hole pockets disappear) [116,164]. Such a correlation with the superconductivity suggests the importance of this hole Fermi surface. However, later, a counter example is found in $Ca_{10}(Pt_4As_8)(Fe_{2-x}Pt_xAs_2)_5$ ($T_c \sim 20$ K), where only d_{xy}-based hole pocket exists [165]. A likely cause is that the d_{xy}-based bands are strongly scattered by Co dopants in $BaFe_{2-x}Co_xAs_2$ and $NaFe_{1-x}Co_xAs$, while it is not strongly scattered in $Ca_{10}(Pt_4As_8)(Fe_{2-x}Pt_xAs_2)_5$. This highlights the effects of impurity on the superconductivity. Furthermore, Cr, Mn, Cu, and Zn dopants at the Fe site kill superconductivity much more effectively than Co and Ni. Their effects on the electronic structure have been extensively studied [166,167].

Electron correlation or, more specifically, spin fluctuations are found to correlate with the superconductivity. It manifests as the distance from the CAF phase, the band renormalization factor, or the dynamical spin susceptibility measured by INS. These general observations suggest that the superconductivity in iron-based superconductors is mediated by magnetic interactions. In a local pairing scenario, the gap functions of various iron-based superconductors were fitted rather well by including exchange interactions between nearest neighbors, the next-nearest neighbors, and the next-to-next-nearest neighbors [168].

So far, a more quantitative correlation between certain electronic properties and superconductivity remains lacking, besides that the SC gap generally scales with T_c. This illustrates the complexity of the problem and requires further systematic work.

$A_xFe_{2-y}Se_2$ and FeSe thin films

$A_xFe_{2-y}Se_2$ and single-layer FeSe thin films grown on the STO substrate are the two known iron-based superconductors with only electron Fermi surface [114,115,169]. Heavily electron-doped iron pnictides have only electron pocket; however, they are non-SC, as the spin fluctuations diminish [121]. These two chalcogenides with unique electronic structure and rather high T_c pose challenges on the physical pictures established previously for systems with both electron and hole Fermi surface sheets.

$A_xFe_{2-y}Se_2$

The SC $A_xFe_{2-y}Se_2$ sample is phase separated, containing iron-vacancy ordered insulating domains and SC domains in nanometer scale, as illustrated in Fig. 12a. The electronic structure of the insulating phase behaves like a Mott insulator. A semiconducting domain was found in some materials, whose band structure is similar to that of the SC domain, except that all the bands are filled. The phase separation was observed both by ARPES and STM, among other measurements [170–173].

For the SC phase, the Fermi surface of $K_xFe_{2-y}Se_2$ is shown in Fig. 12b. The two electron Fermi surfaces around the zone corner cannot be resolved, and there is a small κ electron pocket around Z [114]. The gap distributions on these Fermi surfaces are isotropic as shown in Fig. 12c and d [174]. This and the neutron resonance peak [175] pose severe challenges on theory regarding what kind of pairing symmetry presents in this system.

FeSe/STO thin films

The likely high T_c of 65 K in the single-layer FeSe/STO film has raised a lot of interest [14,115,169]. The largest and isotropic SC gap has been observed by ARPES and STS. The FeSe is found to be doped by electron transferred from the oxygen vacancy states in the STO substrate [115]. The superconductivity is found only in the first layer

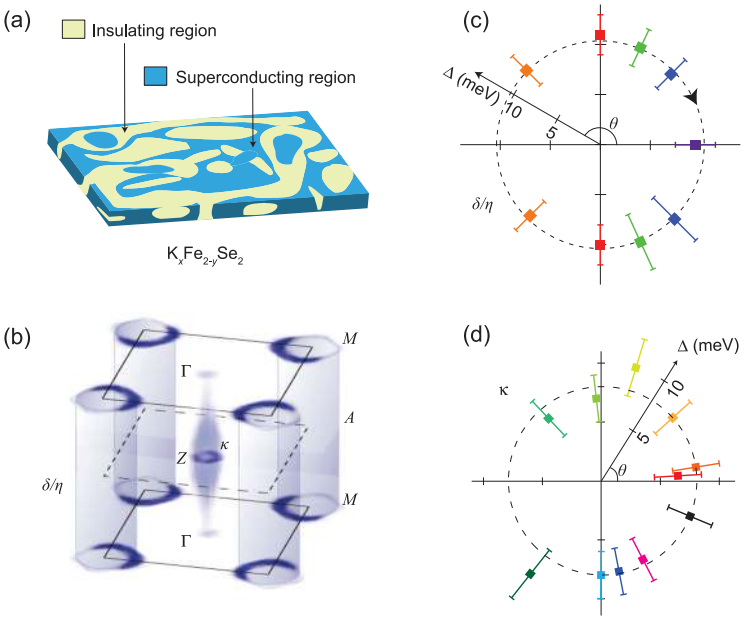

Figure 12. (a) Cartoon for mesoscopic phase separation in SC $K_xFe_{2-y}Se_2$. (b) The Fermi surface of the SC phase. (c) Gap distribution on the δ/η electron pocket around M in polar coordinates, where the radius represents the gap and the polar angle θ represents the position on the δ/η pocket with respect to M, with $\theta = 0$ being the M–Γ direction. (d) is the same as (c), but for the κ pocket. Data are taken from [114,170,174].

on the substrate. For a multi-layer FeSe film, which is undoped, there are both electron and hole Fermi surfaces, and the electronic structure reconstruction corresponding to the CAF order is observed [115].

By further expanding the FeSe lattice with FeSe/STO/KTO heterostructure, the two electron Fermi pockets become more elliptical and resolvable [176]. The lack of hybridization between them and the strong gap anisotropy provide more constraints on theory, suggesting sign change in Fermi sections and inter-band pair–pair interactions [177]. The gap closes around 70 K in FeSe/STO/KTO, even now 75 K for the FeSe/BTO/KTO film [178], indicating a new route to enhance the superconductivity.

The critical role of correlations

Electron correlation is manifested in the band renormalization factor of the iron-based superconductors. Fig. 13(a1) illustrates the evolution of dispersion in $NaFe_{1-x}Co_xAs$; the band becomes much lighter with increased doping. In the heavily electron-doped case, the correlation (or spin fluctuation here) is very weak, as they are far away from the CAF phase. As a result, they are non-SC. However, its Fermi surface is very similar to that of $K_xFe_{2-y}Se_2$, but the latter has a much larger band mass or narrow bandwidth (Fig. 13(a2)), and a T_c around 30 K. The strong correlation in $K_xFe_{2-y}Se_2$ is likely related to its large lattice constant, since for the multi-layer FeSe films, it was found that the CAF ordering strength increases with increased lattice constant (Fig. 13b). These FeSe films are under high tensile strain, whose lattice constants are much larger than that of bulk FeSe [115].

The electronic structure is itinerant in most of the iron-based superconductors. However, there is an effective local moment [134], and the coupling between the itinerant electrons and local moments (which are the two sides of the same coin) gives the Hund's rule coupling, the main correlation source in these compounds [179,180]. Such a Hund's metal behavior is also responsible for the CAF order in these materials. In fact, the energy scale of the electronic structure reconstruction is found to scale with the T_s/T_N and the local moment measured by the neutron scattering, as shown in Fig. 13c [58,115,181–190].

Local moments are important for superconductivity as well. Taking systems like the cT phase as an example, where core-electron spectroscopy indicates the absence of local moments, the superconductivity disappears, and bands become less correlated. The electronic structure of the cT phase is similar to that of $BaFe_2P_2$, where the small lattice constants enhance the hopping and thus the itinerancy. Relatedly, for the single-layer FeSe/STO film or $A_xFe_{2-y}Se_2$, their superconductivity should be related to the enhanced correlations by the expanded lattice.

Assuming that the superconductivity of all the iron-based superconductors is due to one unified mechanism, the results obtained on the above two categories of compounds actually would help to sort out the SC mechanism. The gap is generally isotropic and nodeless (nodes being accidental) in these systems, although there could be sign changes in different Fermi pockets or sections. The dramatic difference in the Fermi surface topologies indicates that the pairing is local in the real space, mediated by short-range AF interactions.

Finally, we note that although a general experimental phenomenology has been established, there are still many remaining open issues to be addressed. For example, in the recent FeSe/STO studies, it was suggested that the interface has a non-trivial role in the superconductivity, and particularly the interfacial phonon might play an important role [178,191].

THEORY

Theory of high-T_c superconductivity remains one of the most fundamental and challenging problems. The BCS theory fails to explain why the SC transition

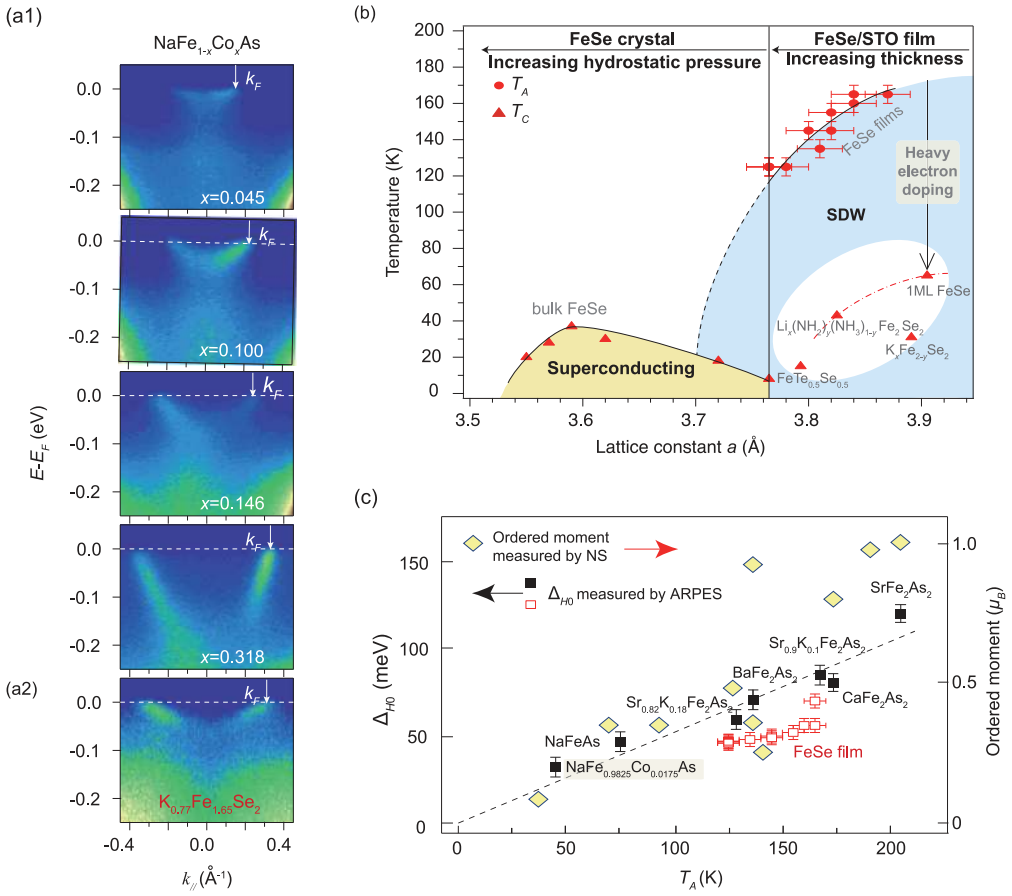

Figure 13. (a1) The doping dependence of an electron-like band η around the zone corner for $NaFe_{1-x}Co_xAs$ with $x = 0.045$, 0.065, 0.146, and 0.318, respectively. (a2) The electron bands around the zone corner of $K_{0.77}Fe_{1.65}Se_2$. Note that the photon energies used for different samples are not the same but all correspond to the same k_z in the 3D Brillouin zone. (b) Phase diagram of FeSe. The T_c and T_A for FeSe are plotted against the lattice constants. The right side is based on thin film ARPES data, and the left side is based on the transport data of FeSe single crystal under hydrostatic pressure taken from [215]. The dashed line represents the extrapolated T_A's, which is the temperature when the band starts to reconstruct or become nematic (i.e. $T_A = T_s'$). Values of T_c's for other iron selenides are also plotted in the elliptical region. (c) Band separation measured by ARPES and ordered moment measured by neutron scattering as a function of T_A. The dashed line is a guide for the eyes. Data in panels (c) and (d) are taken from [115].

temperatures for both cuprate and iron-based superconductors can be much higher than the possible upper limit for electron–phonon-mediated superconductors (40 K) [192]. The highest $T_c \sim 55$ K of iron-based superconductors [6] is still much lower than that for the cuprate superconductors (164 K under high pressure). However, the study for the iron-based superconductivity is of particular interest because (1) Fe^{2+} ions have magnetic moments which are generally believed to be detrimental to superconductivity, and the discovery of high-T_c superconductivity in iron pnictides has overturned this viewpoint and opens a new direction for exploring new superconductors; (2) there are strong AF fluctuations in iron-based superconductors and the investigation to these materials may help us to understand more deeply the pairing mechanism of high-T_c superconductivity in general.

Iron-based superconductors, including iron pnictides and iron chalcogenides, are quasi-2D materials. They have very complicated electronic structures and competing interactions. To understand the mechanism of iron-based superconductivity, the first task is to establish the minimal model to describe the low-energy electronic excitations in these materials. A key issue under debate is whether the system is in the strong or weak coupling limit, since the interaction that drives electrons to pair can be very different in these two limits.

Band structure

From first-principles DFT calculations, we know that the low-energy excitations of electrons in iron-based superconductors are mainly contributed

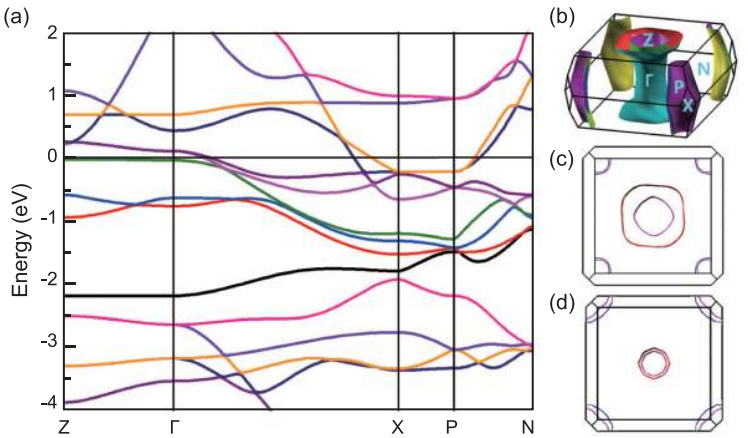

Figure 14. (a) Electronic band structure and (b) band structure in the PM phase for $BaFe_2As_2$ in the folded Brillouin zone. (c) and (d) are the sectional views of the Fermi surface through symmetrical *k*-points *Z* and Γ perpendicular to the *z*-axis, respectively [193].

by Fe 3d electrons. At high temperatures, iron pnictides/chalcogenides are PM metals. At low temperatures, most of parent compounds, including LaFeAsO, $BaFe_2As_2$, and other 1111 and 122 pnictides, and FeTe, are in the AF metallic phase. They become SC upon electron or hole doping. For LaFePO, LiFeAs, or other 111 pnictides, the parent compounds without doping are SC at low temperatures.

As an example, Fig. 14 shows the Fermi surface and the band structure for $BaFe_2As_2$ in the high-temperature PM phase [193]. Similar band structures are found for other iron pnictides [194,195] and chalcogenides [133]. In general, there are five bands across the Fermi surface. Among them are two electron-like Fermi surfaces centered around $M = (\pi, 0)$ and its equivalent points and two hole-like Fermi surfaces centered around the zone center $\Gamma = (0, 0)$. For 1111 or hole-doped 122 materials, in addition to the above four surfaces, there is one more hole-like Fermi surface appearing around *Z*. This band is more 3D like than the other four bands and shows a large energy–momentum dispersion along the *c*-axis. The band structure of the single-layer FeSe grown on the $SrTiO_3$ substrate is relatively simple [196]. There are only two bands, located around $(\pi, 0)$ and $(0, \pi)$, across the Fermi level [197]. The qualitative feature of the band structures obtained by the DFT calculation agrees with the ARPES measurements. But the bandwidth and the effective mass of electrons around the Fermi surface are found to be strongly renormalized by correlation effects which are ignored in the DFT calculation.

Minimal model for describing iron-based superconductivity

Our discussions on minimal model below will be based on strong coupling point of view, where we consider that the electron interaction is strong. The weak coupling viewpoint starts with itinerant electrons and treats electron interaction as a perturbation. The weak coupling theories may explain a number of experiments in iron-based superconductivity [26,27]. However, they have difficulties in explaining local magnetic moments and superconductivity in systems without Fermi surface nesting. Among the five 3d orbitals of Fe ions, d_{xz}, d_{yz}, and d_{xy} contribute most to the low-energy excitations. These orbitals couple strongly with each other and with the other two Fe 3d orbitals, $d_{x^2-y^2}$ and d_{z^2}, by the Hund's rule exchange interaction. In the atomic limit, an Fe^{2+} ion possesses a large magnetic moment, $\sim 4\mu_B$, with a total spin $S = 2$. When Fe atoms form a crystal by hybridizing with As and other atoms, these 3d electrons may become itinerant. If all 3d orbitals of Fe become highly itinerant, one would expect that the magnetic moment of Fe will be completely quenched. However, neutron and other experimental measurements indicate that the magnetic moments of Fe remain finite at least for most of undoped or slightly doped iron pnictides/chalcogenides [58,132,198]. For example, the ordering moment of Fe in the AF ordered state is about $0.37\mu_B$ for LaFeAsO [58], $2\mu_B$ for FeTe [132], and $3.31\mu_B$ for $K_2Fe_4Se_5$ [198]. It should be pointed out that the Fermi surface nesting effect cannot give such a large ordering moment, and the magnetic moment of Fe must have the contribution from electrons whose energy is well below the Fermi level [193]. The total moment of an Fe ion is a sum of the ordering moment and the fluctuating moment. The fluctuating moment results from thermal and quantum fluctuations of Fe moment and is zero on average. A small ordering moment does not mean that the total moment of an Fe spin is also small. The total moments in most of 1111 and 122 pnictides can in fact be much larger than the ordering moments, which suggests strong quantum fluctuation in the parent compounds.

The existence of Fe moments in these materials means that not all Fe 3d electrons are equally conducting, some of them are more localized than the others. From the first-principles density functional calculation, it was found that the crystal splitting of the 3d orbitals is small, but the hybridization between Fe and As/Se atoms and the on-site Coulomb interaction vary differently for different 3d orbitals. This may lead to a Hund's rule coupling assisted

orbital-selective Mott transition [199] and allocate a finite magnetic moment for each Fe by localizing some 3d orbitals. Thus, Fe 3d electrons possess both local and itinerant nature. The low-energy charge dynamics is governed by itinerant 3d electrons and behaves more like in a conventional metal with weak correlation, whereas the spin dynamics is essentially governed by localized moments and behaves more like in a strong coupling system. Moreover, these itinerant electrons and local moment are not independent; they are actually coupled together by the Hund's rule coupling. This is similar as in a colossal magnetoresistance manganate, where the double exchange interaction induced by the Hund's coupling between localized and itinerant electrons is important. Of course, the Coulomb screening of conduction electrons to the local moments is stronger in Fe-based materials. This may explain why the magnetoresistance is fairly large in the AF ordered phase in FeTe or other Fe pnictide materials.

Iron-based materials exhibit various AF orders. These orders are driven predominantly by the magnetic interactions between Fe spins, among them the most important one is the superexchange interaction between Fe spins mediated by As or Se 4p electrons [195]. The superexchange interaction depends on the hybridization between 3d and 4p orbitals, in particular on the bond length and the angle of Fe-As-Fe. Besides this, there is also a direct ferromagnetic exchange interaction between two Fe ions, which is determined by the wavefunction overlap between two 3d orbitals on the two neighboring Fe sites. These exchange interactions are short ranged which extend mainly to the nearest and next-nearest neighbors for Fe pnictides or Fe selenides, and to the third next-nearest neighbors for Fe tellurides [194,195,200].

The above discussion suggests that the minimal model for describing iron-based superconductors is approximately given by [193,199]

$$H = \sum_{ij,\alpha\beta} t_{ij}^{\alpha\beta} c_{\alpha,i}^{\dagger} c_{\beta,j} + J_1 \sum_{\langle ij\rangle} S_i \cdot S_j + J_2 \sum_{\langle\langle ij\rangle\rangle} S_i \cdot S_j, \quad (1)$$

where α and β are the orbital quantum number of itinerant electrons, and $S_i = \sum_\alpha c_{\alpha,i}^{\dagger} \sigma c_{\alpha,i}/2$. The first term is the tight binding Hamiltonian of itinerant electrons. The second and third terms are the exchange interactions between Fe spins on the nearest and next-nearest neighboring sites, respectively. If one ignores the charge fluctuation and considers only the spin dynamics, this Hamiltonian reduces to the $J_1 - J_2$ model [194,195]. In this case, the ground state is CAF ordered if $J_2 > J_1/2$. This is indeed the AF order that is observed by neutron scattering measurements [58] in most of the parent compounds of iron-based superconductors. In passing, we note that the minimal model approximates the spin–spin couplings independent of the five d-orbitals, and has not included Hund's rule interaction.

In iron-based superconductors, the difference between center momenta for the electron and hole bands, i.e. M and Γ, coincides with the characteristic wave vector of the J_2 term. Thus, the J_2 term couples strongly with the electron and hole Fermi surfaces. This term is believed to play an important role in driving both AF and SC orders. If the hole and Fermi surfaces are perfectly nested, then the J_2 coupling will be strongly amplified in the phase space integration, leading to certain Fermi surface nesting effect, such as the SDW instability. Doping can change the phase space that is connected by the nesting vector, which can strengthen the SC order and weaken the AF order, or vice versa. In general, the competition between SC and AF correlations is strong in these materials. The SC order emerges when the AF order is suppressed.

Gap symmetry and structure

In a SC phase, quantum fluctuations are suppressed by the SC long-range order and the BCS mean field approximation is valid. The pairing gap of electrons is an order parameter characterizing a SC state. Physical properties in a SC state can be well described by the BCS theory once the gap function is known. This is the reason why the gap function is of particular interest for study. While a non-s-wave symmetry may indicate unlikely phonon-mediated pairing, the pairing symmetry alone is not sufficient to determine the pairing interaction.

The gap symmetry is determined by the pairing interaction. If the pairing is induced by electron–phonon interaction, it is generally expected that the energy gap has s-wave symmetry. On the other hand, if the pairing is induced by AF fluctuations, a spin singlet d-wave (for example in high-T_c cuprates) or spin triplet p-wave (for example in Sr_2RuO_4) pairings are possible, depending strongly on the band structure, especially on the structure of Fermi surfaces. This is because the SC pairing is a low-energy effect and involves only excitations of electrons around the Fermi surface. For the same pairing interaction, the gap symmetry may change with the change of the Fermi surface.

The gap symmetry is classified according to the point group of crystal. Theoretical study suggested that the pairing gap of iron-based superconductors has conventional s-wave symmetry [151,201–203],

namely in the identity representation of point group. This has been confirmed by spectroscopy and transport measurements on most of iron-based superconductors including $Ba_{1-x}K_xFe_2As_2$, $BaFe_{2-x}Co_xAs_2$, $KxFe_{2-x}Se_2$, and $FeTe_{1-x}Se_x$. However, for KFe_2As_2, $BaFe_{2-x}Ru_xAs_2$, and nearly all phosphorus-based superconductors, LaFePO, LiFeP, and $BaFe_2As_{2-x}P_x$, it was found that gap nodes exist. The presence of gap nodes generally implies that the pairing symmetry is unconventional, although an extended s-wave pairing may have accidental nodes on one or more Fermi surfaces.

Fe-based superconductors are multi-band systems. There are several bands across the Fermi level. Even if we assume that the pairing has s-wave symmetry, the relative phases of gap functions can be different on different Fermi surfaces, depending on inter-band pairing amplitudes to be attractive or repulsive. If the gap function has the same phase on all the Fermi surfaces, the pairing is said to have s^{++} symmetry. On the other hand, if the gap function has opposite phases on different Fermi surfaces, the pairing is said to have s^{+-} symmetry.

The relative phase of the gap function is determined by the interaction between Cooper pairs on different bands. For iron-based superconductors, if the pairing is induced by the AF fluctuations, interaction between Cooper pairs on the electron and hole bands will generally be repulsive. In this case, the SC phases are opposite on the hole and electron Fermi surface, and the gap function has s^{+-} symmetry [151,201–204]. However, if the pairing is induced by the orbital fluctuation and the SC instability happens in the A_{1g} channel, the interaction between Cooper pairs on the electron and hole bands is attractive, and the gap function will have s^{++} symmetry [205]. Thus, from the relative phases in the gap function, one can determine whether the SC pairs are glued by AF fluctuations or by orbital fluctuations.

In the literature, there are quite many discussions on the phase structure of the gap function. However, this phase structure is not in the angular orientation and is not sensitive to most experiments. It is actually very difficult to resolve unambiguously this seemly simple phase problem [206]. For an s^{+-} superconductor, it is expected that a strong neutron resonance peak exists around the momentum linking hole and electron Fermi surfaces, i.e. at $M = (\pi, 0)$ and equivalent points. This resonance peak has in fact been observed in nearly all iron-based superconductors [207,208], lending strong support to the theory that predicts the pairing to have s^{+-} symmetry. From the experimental observation of quantum interference of quasi-particles with magnetic or non-magnetic impurities, it was also found that an s^{+-} pairing is more likely [152]. On the other hand, from Anderson's theorem, it is well known that non-magnetic impurity scattering does not affect much the transition temperature for s^{++} superconductors, but it may reduce strongly the transition temperature for s^{+-} superconductors. In particular, the transition temperature of an s^{+-} superconductor should decrease with increasing impurity concentration. However, for iron-based superconductors, the critical transition temperature does not depend much on the quality of samples. This seems to suggest that the s^{++} pairing is more favored. More systematic study of various impurity effects provides mixed information [209], which may suggest non-universal behavior on the relative phases in iron-based superconductors, in contrast to the universal d-wave pairing in high-T_c cuprates.

The SC and AF orders are two competing orders. Generally they repel each other. However, if the pairing has s^{+-} symmetry, theoretical calculation suggested that these two kinds of orders can coexist [210]. Experimentally, this kind of coexistence has indeed been observed in $BaFe_2As_2$, $Ba_{1-x}K_xFe_2As_2$, and $SmFeAsO_{1-x}F_x$ with Co substituting Fe or with P substituting As [73,211], and in $K_xFe_2Se_2$. But in these systems in which the coexistence was observed, the SC gap was also found to have line nodes. It is unknown whether the coexistence is caused by the s^{+-} pairing symmetry or by the line nodes, or the other way around.

SUMMARY AND PERSPECTIVE

In this article, we have reviewed a number of physical properties of iron-based superconductors. During the past six years, tremendous progress has been achieved in the synthesis of materials, growth of single crystals, characterization of crystal structures, measurements of thermodynamics, and transport and various spectroscopic quantities for iron-based superconductors. This has given us a comprehensive understanding on the chemical and crystal structures, band structures, spin and orbital orderings, pairing symmetry, and other physical properties of iron-based superconductors. In particular, the normal states of Fe-based superconductors have multiple Fermi surfaces including electron Fermi pockets and hole Fermi pockets. This indicates importance of multi-orbitals in these materials. Fe-based superconductors are proximate to antiferromagnetism, which suggests that AF fluctuations are responsible for the observed superconductivity.

Studies on the mechanism of iron-based superconductivity are an important part of research on the mechanism of high-T_c superconductivity. Any progress in this direction may have strong impact

on the study of theory of strongly correlated quantum systems. To investigate the SC mechanism, one needs to find out the microscopic origin that causes the pairing of electrons and establish a theory that is capable of explaining existing experimental data and predicting new experimental effects. This remains a challenging task. Similar to the cuprate superconductivity, iron-based superconductivity is generally believed to originate predominantly from the electron–electron repulsive interaction, which induces AF fluctuations. Superconductivity induced by AF fluctuation has recently been reviewed by Scalapino [69]. In the present theories based on AF fluctuation, one approximates the pairing vertex solely in terms of the exchange of AF fluctuations. This should be reasonable in some cases such as heavy fermion superconductivity, where the SC state is near the AF quantum critical point. In cuprates, there is also the Mott physics. In iron-based SC materials, we have argued that the systems are in strong coupling limit. Furthermore, the system may well have orbital-selected Mott physics. Theoretical description of high-T_c superconductivity in both cuprate and iron-based superconductivity remains a great challenge.

Iron-based superconductors are multi-band materials. All five 3d orbitals of Fe hybridize strongly with As or Se 4p orbitals. They also couple strongly with each other and have contribution to both itinerant conducting electrons and localized magnetic moments. This brings much complexity to the understanding and explanation of experimental phenomena. We are lacking a clear physical picture with reliable theoretical tools to treat an electronic system with strong coupling between itinerant and localized electrons. Theoretical study for iron-based superconductors relies more on phenomenological analysis of experimental observations and on various approximations.

In short, the iron-based SC mechanism is a challenging problem. To solve this problem, we need to further improve the quality of single crystals and the resolution of measurements. Besides the routine measurements and characterizations, it is more important to design and carry out smoking gun experimental measurements to solve a number of key problems, for example the problem whether the gap function has the s^{+-} symmetry. This will reduce greatly the blindness in the theoretical study and leads to a thorough understanding of iron-based superconductivity.

Fe-based materials have highest SC T_c next to cuprate. Their discovery has greatly encouraged the search for other superconductors with higher T_c. While we are still far from the stage to predict high-T_c materials, there is good progress along this development. It is possible in future that theory may guide the search or synthesis of the high-T_c superconductors.

ACKNOWLEDGEMENTS

We thank our collaborators in high-T_c superconductivity and the colleagues attending Beijing Forum of High-T_c for numerous stimulating discussions over the years. Xianhui Chen, Donglai Feng, and Fu-Chun Zhang would like to thank Collaborative Innovation Center of Advanced Microstructures, Nanjing, China. We wish to acknowledge Yan Zhou and Xingye Lu for their helpful assistance in the preparation of this manuscript.

FUNDING

This work is in part supported by National Science Foundation of China and Ministry of Science and Technology. Pengcheng Dai is also supported by the US NSF DMR-1308603 and OISE-0968226.

REFERENCES

1. Bednorz, JG and Muller, KA. Possible high T_C superconductivity in the BaLaCuO system. *Z Phys B* 1986; **64**: 189–93.
2. Wu, MK, Ashburn, JR and Torng, CJ *et al.* Superconductivity at 93 K in a new mixed-phase YBaCuO compound system at ambient pressure. *Phys Rev Lett* 1987; **58**: 908.
3. Kamihara, Y, Watanabe, T and Hirano, M *et al.* Iron-based layered superconductor $LaO_{1-x}F_xFeAs$ (x = 0.05-0.12) with Tc = 26 K. *J Am Chem Soc* 2008; **130**: 3296.
4. Chen, XH, Wu, T and Wu, G *et al.* Superconductivity at 43 K in $SmFeAsO_{1-x}F_x$. *Nature* 2008; **453**: 761–2.
5. Chen, GF, Li, Z and Wu, Z *et al.* Superconductivity at 41 K and its competition with spin-density-wave instability in layered $CeO_{1-x}F_xF'eAs$. *Phys Rev Lett* 2008; **100**: 247002.
6. Ren, ZA, Lu, W and Yang, J *et al.* Superconductivity at 55 K in iron-based F-doped layered quaternary compound $SmO_{1-x}F_xFeAs$. *Chin Phys Lett* 2008; **25**: 2215.
7. Ren, ZA, Yang, J and Lu, W *et al.* Superconductivity in the iron-based F-doped layered quaternary compound $NdO_{1-x}F_xFeAs$. *Europhys Lett* 2008; **82**: 57002.
8. Wang, C, Li, L and Chi, S *et al.* Thorium-doping-induced superconductivity up to 56 K in $Gd_{1-x}Th_xFeAsO$. *Europhys Lett* 2008; **83**: 67006.
9. Wen, HH, Mu, G and Fang, L *et al.* Superconductivity at 25 K in hole-doped $(La_{1-x}Srh_x)OFeAs$. *Europhys Lett* 2008; **82**: 17009.
10. Rotter, M, Tegel, M and Johrendt, D. Superconductivity at 38 K in the iron arsenide $(Ba_{1-x}K_x)Fe_2As_2$. *Phys Rev Lett* 2008; **101**: 107006.
11. Hsu, FC, Luo, JY and Yeh, KW *et al.* Superconductivity in the PbO-type structure α-FeSe. *Proc Natl Acad Sci USA* 2008; **105**: 14262–4.
12. Wang, XC, Liu, QQ and Lv, YX *et al.* The superconductivity at 18 K in LiFeAs system. *Solid State Commun* 2008; **148**: 538–40.
13. Parker, DR, Pitcher, MJ and Baker, PJ *et al.* Structure, antiferromagnetism and superconductivity of the layered iron arsenide NaFeAs. *Chem Commun* 2009; **2009**: 2189–91.

14. Wang, QY, Li, Z and Zhang, WH *et al.* Interface-induced high-temperature superconductivity in single unit-cell FeSe films on $SrTiO_3$. *Chin Phys Lett* 2012; **29**: 037402.
15. Anderson, PW. The resonating valence bond state in Lah_2CuOh_4 and superconductivity. *Science* 1987; **235**: 1196–8.
16. Anderson, PW, Lee, PA and Randeria, M *et al.* The physics behind high-temperature superconducting cuprates: the 'plain vanilla' version of RVB. *J Phys-Condens Matter* 2004; **16**: R755–69.
17. Lee, PA, Nagaosa, N and Wen, XG. Doping a Mott insulator: physics of high-temperature superconductivity. *Rev Mod Phys* 2006; **78**: 17–85.
18. Rice, TM, Yang, KY and Zhang, FC. A phenomenological theory of the anomalous pseudogap phase in underdoped cuprates. *Rep Prog Phys* 2012; **75**: 016502.
19. Haule, K, Shim, JH and Kotliar, G. Correlated electronic structure of $LaO_{1-x}F_xAs$. *Phys Rev Lett* 2008; **100**: 226402.
20. Zhang, FC and Rice, TM. Effective Hamiltonian for superconducting copper oxides. *Phys Rev B* 1988; **37**: 3759–61.
21. Johnston, DC. The puzzle of high temperature superconductivity in layered iron pnictides and chalcogenides. *Adv Phys* 2010; **59**: 803–1061.
22. Stewart, GR. Superconductivity in iron compounds. *Rev Mod Phys* 2011; **83**: 1589–652.
23. Dagotto, E. The unexpected properties of alkali metal iron selenide superconductors. *Rev Mod Phys* 2013; **85**: 849–67.
24. Dai, PC, Hu, JP and Dagotto, E. Magnetism and its microscopic origin in iron-based high-temperature superconductors. *Nat Phys* 2012; **8**: 709–18.
25. Paglinone, J and Greene, RL. High-temperature superconductivity in iron-based materials. *Nat Phys* 2010; **6**: 645–58.
26. Hirschfeld, PJ, Korshunov, MM and Mazin, II. Gap symmetry and structure of Fe-based superconductors. *Rep Prog Phys* 2011; **74**: 124508.
27. Chubukov, AV. Paring mechanism in Fe-based superconductors. *Annu Rev Condens Matter Phys* 2012; **3**: 57–92.
28. Wang, AF, Luo, XG and Yan, YJ *et al.* Phase diagram and calorimetric properties of $NaFe_{1-x}Co_xAs$. *Phys Rev B* 2012; **85**: 224521.
29. Izyumov, YA and Kurmaev, EZ. FeAs systems: a new class of high-temperature superconductors. *Phys-Usp* 2008; **51**: 1261–86.
30. Tegel, M, Johansson, S and Weiss, V *et al.* Synthesis, crystal structure and spin-density-wave anomaly of the iron arsenide-fluoride SrFeAsF. *Europhys Lett* 2008; **84**: 67007.
31. Matsuishi, S, Inoue, Y and Nomura, T *et al.* Superconductivity induced by co-doping in quaternary fluoroarsenide CaFeAsF. *J Am Chem Soc* 2008; **130**: 14428–29.
32. Hanna, T, Muraba, Y and Matsuishi, S *et al.* Hydrogen in layered iron arsenides: indirect electron doping to induce superconductivity. *Phys Rev B* 2011; **84**: 024521.
33. Matsuishi, S, Inoue, Y and Nomura, T *et al.* Effect of 3d transition metal doping on the superconductivity in quaternary fluoroarsenide CaFeAsF. *New J Phys* 2009; **11**: 025012.
34. Takahashi, H, Tomita, T and Soeda, H *et al.* High-pressure studies for hydrogen substituted $CaFeAsF_{1-x}H_x$ and $SmFeAsO_{1-x}H_x$. *J Supercond Nov Mag* 2012; **25**: 1293.
35. Wu, G, Xie, YL and Chen, H *et al.* Superconductivity at 56 K in samarium-doped SrFeAs. *J Phys-Condens Matter* 2009; **21**: 142203.
36. Lu, XF, Wang, NZ and Zhang, GH *et al.* Superconductivity in $LiFeO_2Fe_2Se_2$ with anti-PbO-type spacer layers. *Phys Rev B* 2013; **89**: 020507 (R).
37. Wu, G, Chen, H and Wu, T *et al.* Different resistivity response to spin density wave and superconductivity at 20 K in $Ca_{1-x}Na_xFe_2As_2$. *J Phys-Condens Matter* 2008; **20**: 422201.
38. Ronning, F, Klimczuk, T and Bauer, ED *et al.* Synthesis and properties of $CaFe_2As_2$ single crystals. *J Phys-Condens Matter* 2008; **20**: 322201.
39. Sasmal, K, Lv, B and Lorenz, B *et al.* Superconducting Fe-based compounds $(A_{1-x}Sr_x)Fe_2As_2$ with A=K and Cs with transition temperatures up to 37 K. *Phys Rev Lett* 2008; **101**: 107007.
40. Guo, J, Jin, S and Wang, G *et al.* Superconductivity in the iron selenide $K_xFe_2Se_2$ ($0 \leq x \leq 1.0$). *Phys Rev B* 2010; **82**: 180520 (R).
41. Krzton-Maziopa, A, Shermadini, Z and Pomjakushina, E *et al.* Synthesis and crystal growth of $Cs_{0.8}(FeSe_{0.98})_2$: a new iron-based superconductor with $T_c = 27$ K. *J Phys-Condens Matter* 2011; **23**: 052203.
42. Wang, AF, Ying, JJ and Yan, YJ *et al.* Superconductivity at 32 K in single-crystalline $Rb_xFe_{2-y}Se_2$. *Phys Rev B* 2011; **83**: 060512.
43. Fang, MH, Wang, HD and Dong, CH *et al.* Fe-based superconductivity with T_c=31 K bordering an antiferromagnetic insulator in $(Tl,K)Fe_xSe_2$. *Europhys Lett* 2011; **94**: 27009.
44. Lv, B, Deng, LZ and Gooch, M *et al.* Unusual superconducting state at 49 K in electron-doped $CaFe_2As_2$ at ambient pressure. *Proc Natl Acad Sci USA* 2011; **108**: 15705–9.
45. Yakita, H, Ogino, H and Okada, T *et al.* A new layered iron arsenide superconductor: $(Ca,Pr)FeAs_2$. *J Am Chem Soc* 2014; **136**: 846–9.
46. Ying, TP, Chen, XL and Wang, G *et al.* Observation of superconductivity at 30 $\sim$ 46 K in $A_xFe_2Se_2$ (A = Li, Na, Ba, Sr, Ca, Yb, and Eu). *Sci Rep* 2010; **2**: 426.
47. Burrard-Lucas, M, Free, DG and Sedlmaier, SJ *et al.* Enhancement of the superconducting transition temperature of FeSe by intercalation of a molecular spacer layer. *Nat Mater* 2013; **12**: 15–9.
48. Scheidt, EW, Hathwar, VR and Schmitz, D *et al.* Superconductivity at $T_c = 44$ K in $Li_xFe_2Se_2(NH_3)_y$. *Eur J Phys B* 2012; **85**: 279.
49. Krzton-Maziopa, A, Pomjakushin, EV and Pomjakushin, VY *et al.* Synthesis of a new alkali metal-organic solvent intercalated iron selenide superconductor with $T_c \sim 45$ K. *J Phys-Condens Matter* 2012; **24**: 382202.
50. Zhu, XY, Han, F and Mu, G *et al.* $Sr_3Sc_2Fe_2As_2O_5$ as a possible parent compound for FeAs-based superconductors. *Phys Rev B* 2009; **79**: 024516.
51. Xie, YL, Liu, RH and Wu, T *et al.* Structure and physical properties of the new layered oxypnictides $Sr_4Sc_2O_6M_2As_2$ (M=Fe and Co). *Europhys Lett* 2009; **86**: 57007.
52. Ogino, H, Sato, S and Kishio, K *et al.* Homologous series of iron pnictide oxide superconductors with extremely thick blocking layers. *Appl Phys Lett* 2010; **97**: 072506.
53. Ogino, H, Machida, K and Yamamoto, A *et al.* A new homologous series of iron pnictide oxide superconductors $(Fe_2As_2)(Ca_{n+2}(Al, Ti)_nO_y)$ (n = 2, 3, 4). *Supercond Sci Tech* 2010; **23**: 115005.
54. Ogino, H, Shimizu, Y and Ushiyama, K *et al.* Superconductivity above 40 K observed in a new iron arsenide oxide $(Fe_2As_2)(Ca_4(Mg,Ti)_3O_y)$. *Appl Phys Express* 2010; **3**: 063103.
55. Kakiya, S, Kudo, K and Nishikubo, Y *et al.* Superconductivity at 38 K in iron-based compound with platinum-arsenide layers $Ca_{10}(Pt_4As_8)(Fe_{2-x}Pt_xAs_2)_5$. *J Phys Soc Jpn* 2011; **80**: 093704.
56. Ni, N, Jared, MA and Chan, BC *et al.* High T_c electron doped $Ca_{10}(Pt_3As_8)(Fe_2As_2)_5$ and $Ca_{10}(Pt_4As_8)(Fe_2As_2)_5$ superconductors with skutterudite intermediary layers. *Proc Natl Acad Sci USA* 2011; **108**: E1019–26.

57. Sun, YL, Jiang, H and Zhai, HF *et al.* $Ba_2Ti_2Fe_2As_4O$: a new superconductor containing Fe_2As_2 layers and Ti_2O sheets. *J Am Chem Soc* 2012; **134**: 12893–6.
58. De la Cruz, C, Huang, Q and Lynn, JW *et al.* Magnetic order close to superconductivity in the iron-based layered $LaO_{1-x}F_xFeAs$ systems. *Nature* 2008; **453**: 899–902.
59. Nomura, T, Kim, SW and Kamihara, Y *et al.* Crystallographic phase transition and high-T_c superconductivity in LaFeAsO:F. *Supercond Sci Tech* 2008; **21**: 125028.
60. Luo, YK, Tao, Q and Li, YK *et al.* Evidence of magnetically driven structural phase transition in RFeAsO (R=La, Sm, Gd, and Tb): a low-temperature x-ray diffraction study. *Phys Rev B* 2009; **80**: 224511.
61. Margadonna, S, Takabayashi, Y and McDonald, MT *et al.* Crystal structure and phase transitions across the metal-superconductor boundary in the $SmFeAsO_{1-x}F_x$ ($0 \leq x \leq 0.20$) family. *Phys Rev B* 2009; **79**: 014503.
62. Huang, Q, Qiu, Y and Bao, W *et al.* Neutron-diffraction measurements of magnetic order and a structural transition in the parent $BaFe_2As_2$ compound of FeAs-based high-temperature superconductors. *Phys Rev Lett* 2008; **101**: 257003.
63. Mizuguchi, Y, Hara, Y and Deguchi, K *et al.* Anion height dependence of T_c for the Fe-based superconductor. *Supercond Sci Tech* 2010; **23**: 054013.
64. Lee, CH, Kihou, K and Iyo, A *et al.* Relationship between crystal structure and superconductivity in iron-based superconductors. *Solid State Commun* 2012; **152**: 644–8.
65. Zhao, J, Huang, Q and de la Cruz, C *et al.* Structural and magnetic phase diagram of $CeFeAsO_{1-x}F_x$ and its relation to high-temperature superconductivity. *Nat Mater* 2008; **7**: 953–9.
66. Shirage, PM, Miyazawa, K and Ishikado, M *et al.* High-pressure synthesis and physical properties of new iron (nickel)-based superconductors. *Physica C* 2013; **469**: 355–69.
67. Dong, J, Zhang, HJ and Xu, G *et al.* Competing orders and spin-density-wave instability in $La(O_{1-x}F_x)FeAs$. *Europhys Lett* 2008; **83**: 27006.
68. Uemura, YJ. Commonalities in phase and mode. *Nat Mater* 2009; **8**: 253–5.
69. Scalapino, DJ. A common thread: the pairing interaction for unconventional superconductors. *Rev Mod Phys* 2012; **84**: 1383.
70. Kim, MG, Kreyssig, A and Lee, YB *et al.* Commensurate antiferromagnetic ordering in $Ba(Fe_{1-x}Co_x)_2As_2$ determined by x-ray resonant magnetic scattering at the Fe *K* edge. *Phys Rev B* 2010; **82**: 180412 (R).
71. Wang, MY, Luo, HQ and Zhao, J *et al.* Electron-doping evolution of the low-energy spin excitations in the iron arsenide superconductor $BaFe_{2-x}Ni_xAs_2$. *Phys Rev B* 2010; **81**: 174524.
72. Wang, MY, Luo, HQ and Wang, M *et al.* Magnetic field effect on static antiferromagnetic order and spin excitations in the underdoped iron arsenide superconductor $BaFe_{1.92}Ni_{0.08}As_2$. *Phys Rev B* 2011; **83**: 094516.
73. Nandi, S, Kim, MG and Kreyssig, A *et al.* Anomalous suppression of the orthorhombic lattice distortion in superconducting $Ba(Fe_{1-x}Co_x)_2As_2$ single crystals. *Phys Rev Lett* 2010; **104**: 057006.
74. Pratt, DK, Kim, MG and Kreyssig, A *et al.* Incommensurate spin-density wave order in electron-doped $BaFe_2As_2$ superconductors. *Phys Rev Lett* 2011; **106**: 257001.
75. Luo, HQ, Zhang, R and Laver, M *et al.* Coexistence and competition of the short-range incommensurate antiferromagnetic order with the superconducting state of $BaFe_{2-x}Ni_xAs_2$. *Phys Rev Lett* 2012; **108**: 247002.
76. Lu, XY, Gretarsson, H and Zhang, R *et al.* Avoided quantum criticality and magnetoelastic coupling in $BaFe_{2-x}Ni_xAs_2$. *Phys Rev Lett* 2013; **110**: 257001.
77. Avci, S, Chmaissem, O and Chung, DY *et al.* Phase diagram of $Ba_{1-x}K_xFe_2As_2$. *Phys Rev B* 2012; **85**: 184507.
78. Li, L, Luo, Y and Wang, QB *et al.* Superconductivity induced by Ni doping in $BaFeh_2Ash_2$ single crystals. *New J Phys* 2009; **11**: 025008.
79. Rotter, M, Pangerl, M and Tegel, M *et al.* Superconductivity and crystal structures of $(Bah_{1-x}Kh_x)Feh_2ASh_2$ (x=0-1). *Angew Chem Int Ed* 2008; **47**: 7949.
80. Harriger, LW, Luo, HQ and Liu, MS *et al.* Nematic spin fluid in the tetragonal phase of $BaFeh_2Ash_2$. *Phys Rev B* 2011; **84**: 054544.
81. Liu, MS, Harriger, LW and Luo, HQ *et al.* Nature of magnetic excitations in superconducting $BaFeh_{1.9}Nih_{0.1}Ash_2$. *Nat Phys* 2012; **8**: 376.
82. Luo, HQ, Lu, XY and Zhang, R *et al.* Electron doping evolution of the magnetic excitations in $BaFeh_{2-x}Nih_xAsh_2$. *Phys Rev B* 2013; **88**: 144516.
83. Wang, M, Zhang, CL and Lu, XY *et al.* Doping dependence of spin excitations and its correlations with high-temperature superconductivity in iron pnictides. *Nat Commun* 2013; **4**: 2874.
84. Zhang, CL, Wang, M and Luo, HQ *et al.* Neutron scattering studies of spin excitations in hole-doped $Bah_{0.67}Kh_{0.33}Feh_2Ash_2$ superconductor. *Sci Rep* 2011; **1**: 115.
85. Castellan, JP, Rosenkranz, S and Goremychkin, EA *et al.* Effect of Fermi surface nesting on resonant spin excitations in $Bah_{1-x}Kh_xFeh_2Ash_2$. *Phys Rev Lett* 2011; **107**: 177003.
86. Lee, CH, Kihou, K and Kawano-Furukawa, H *et al.* Incommensurate spin fluctuations in hole-overdoped superconductor KFe_2As_2. *Phys Rev Lett* 2011; **106**: 067003.
87. Zhao, J, Adroja, DT and Yao, DX *et al.* Spin waves and magnetic exchange interactions in $CaFeh_2Ash_2$. *Nat Phys* 2009; **5**: 555.
88. Christianson, AD, Goremychkin, EA and Osborn, R *et al.* Unconventional superconductivity in $Bah_{0.6}Kh_{0.4}Feh_2Ash_2$ from inelastic neutron scattering. *Nature* 2008; **456**: 930.
89. Lumsden, MD, Christianson, AD and Parshall, D *et al.* Two-dimensional resonant magnetic excitation in $BaFeh_{1.84}Coh_{0.16}Ash_2$. *Phys Rev Lett* 2009; **102**: 107005.
90. Chi, SX, Schneidewind, A and Zhao, J *et al.* Inelastic neutron-scattering measurements of a three-dimensional spin resonance in the FeAs-based $BaFeh_{1.9}Nih_{0.1}Ash_2$ superconductor. *Phys Rev Lett* 2009; **102**: 107006.
91. Li, SL, Chen, Y and Chang, S *et al.* Spin gap and magnetic resonance in superconducting $BaFe_{1.9}Ni_{0.1}As_2$. *Phys Rev B* 2009; **79**: 174527.
92. Eschrig, M. The effect of collective spin-1 excitations on electronic spectra in high-T_c superconductors. *Adv Phys* 2006; **55**: 47–183.
93. Park, JT, Inosov, DS and Yaresko, A *et al.* Symmetry of spin excitation spectra in the tetragonal paramagnetic and superconducting phases of 122-ferropnictides. *Phys Rev B* 2010; **82**: 134503.
94. Zhou, KJ, Huang, YB and Monney, C *et al.* Persistent high-energy spin excitations in iron-pnictide superconductors. *Nat Commun* 2013; **4**: 1470.
95. Lester, C, Chu, JH and Analytis, JG *et al.* Dispersive spin fluctuations in the nearly optimally doped superconductor $Ba(Fe_{1-x}Co_x)_2As_2$ (x=0.065). *Phys Rev B* 2010; **81**: 064505.
96. Bardeen, J, Cooper, LN and Schrieffer, JR. Theory of superconductivity. *Phys Rev* 1957; **108**: 1175–204.
97. Chester, GV. Difference between normal and superconducting states of a metal. *Phys Rev* 1956; **103**: 1693–9.
98. Schrieffer, JR. *Theory of Superconductivity*. New York, NY: Perseus Books, 1999.
99. Tranquada, JM, Xu, GY and Zaliznyak, IA. Superconductivity, antiferromagnetism, and neutron scattering. *J Magn Magn Mater* 2014; **350**: 148.

100. Headings, NS, Hayden, SM and Coldea, R *et al.* Anomalous high-energy spin excitations in the high-T_c superconductor-parent antiferromagnet La_2CuO_4. *Phys Rev Lett* 2010; **105**: 247001.
101. Demler, E and Zhang, SC. Quantitative test of a microscopic mechanism of high-temperature superconductivity. *Nature* 1998; **396**: 733–5.
102. Woo, H, Dai, PC and Hayden, SM *et al.* Magnetic energy change available to superconducting condensation in optimally doped $YBa_2Cu_3O_6$.95. *Nat Phys* 2006; **2**: 600–4.
103. Dahm, T, Hinkov, V and Borisenko, SV *et al.* Strength of the spin-fluctuation-mediated pairing interaction in a high-temperature superconductor. *Nat Phys* 2009; **5**: 217–21.
104. Stockert, O, Arndt, J and Faulhaber, E *et al.* Magnetically driven superconductivity in $CeCu_2Si_2$. *Nat Phys* 2011; **7**: 119–24.
105. Ning, FL, Ahilan, K and Imai, T *et al.* Contrasting spin dynamics between underdoped and overdoped $Ba(Fe_{1-x}Co_x)_2As_2$. *Phys Rev Lett* 2010; **104**: 037001.
106. Soh, JH, Tucker, GS and Pratt, DK *et al.* Inelastic neutron scattering study of a nonmagnetic collapsed tetragonal phase in nonsuperconducting $CaFe_2As_2$: evidence of the impact of spin fluctuations on superconductivity in the iron-arsenide compounds. *Phys Rev Lett* 2013; **111**: 227002.
107. Ma, FJ and Lu, ZY. Iron-based layered compound LaFeAsO is an antiferromagnetic semimetal. *Phys Rev B* 2008; **78**: 033111.
108. Yang, LX, Zhang, Y and Ou, HW *et al.* Electronic structure and unusual exchange splitting in the spin-density-wave state of the $BaFe_2As_2$ parent compound of iron-based superconductors. *Phys Rev Lett* 2009; **102**: 107002.
109. Yang, LX, Xie, BP and Zhang, Y *et al.* Surface and bulk electronic structures of LaFeAsO studied by angle-resolved photoemission spectroscopy. *Phys Rev B* 2010; **82**: 104519.
110. He, C, Zhang, Y and Xie, BP *et al.* Electronic-structure-driven magnetic and structure transitions in superconducting NaFeAs single crystals measured by angle-resolved photoemission spectroscopy. *Phys Rev Lett* 2010; **105**: 117002.
111. Zhang, Y, Chen, F and He, C *et al.* Strong correlations and spin-density-wave phase induced by a massive spectral weight redistribution in α-$Fe_{1.06}Te$. *Phys Rev B* 2010; **82**: 165113.
112. Chen, F, Zhou, B and Zhang, Y *et al.* Electronic structure of $Fe_{1.04}Te_{0.66}Se_{0.34}$. *Phys Rev B* 2010; **81**: 014526.
113. Zhao, L, Mou, DX and Liu, SY *et al.* Common Fermi-surface topology and nodeless superconducting gap of $K_{0.68}Fe_{1.79}Se_2$ and $(Tl_{0.45}K_{0.34})Fe_{1.84}Se_2$ superconductors revealed via angle-resolved photoemission. *Phys Rev B* 2011; **83**: 140508 (R).
114. Zhang, Y, Yang, LX and Xu, M *et al.* Nodeless superconducting gap in $A_xFe_2Se_2$(A = K,Cs) revealed by angle-resolved photoemission spectroscopy. *Nat Mater* 2011; **10**: 273.
115. Tan, SY, Zhang, Y and Xia, M *et al.* Interface-induced superconductivity and strain-dependent spin density waves in FeSe/$SrTiO_3$ thin films. *Nat Mater* 2013; **12**: 634.
116. Ye, ZR, Zhang, Y and Xu, M *et al.* Orbital selective correlations between nesting/scattering/Lifshitz transition and the superconductivity in $AFe_{1-x}Co_xAs$(A = Li, Na). *arXiv* 2013; 1303.0682.
117. Singh, DJ. Electronic structure of Fe-based superconductors. *Physica C* 2009; **469**: 418.
118. Zhang, Y, Chen, F and He, C *et al.* Orbital characters of bands in the iron-based superconductor $BaFe_{1.85}Co_{0.15}As_2$. *Phys Rev B* 2011; **83**: 054510.
119. Mazin, II and Schmalian, J. Pairing symmetry and pairing state in ferropnictides: theoretical overview. *Physica C* 2009; **469**: 614.
120. Ye, ZR, Zhang, Y and Chen, F *et al.* Doping dependence of the electronic structure in phosphorus-doped ferropnictide superconductor $BaFe_2(As_{1-x}P_x)_2$ studied by angle-resolved photoemission spectroscopy. *Phys Rev B* 2012; **86**: 035136.
121. Sato, T, Nakayama, K and Sekiba, Y *et al.* Band structure and Fermi surface of an extremely overdoped iron-based superconductor KFe_2As_2. *Phys Rev Lett* 2009; **101**: 047002.
122. Dhaka, RS, Liu, C and Fernandes, RM *et al.* What controls the phase diagram and superconductivity in Ru-substituted $BaFe_2As_2$. *Phys Rev Lett* 2011; **107**: 267002.
123. Ishida, S, Nakajima, M and Liang, T *et al.* Anisotropy of the in-plane resistivity of underdoped $Ba(Fe_{1-x}Co_x)_2As_2$ superconductors induced by impurity scattering in the antiferromagnetic orthorhombic phase. *Phys Rev Lett* 2013; **110**: 207001.
124. Zhang, Y, Ye, ZR and Ge, QQ *et al.* Nodal superconducting-gap structure in ferropnictide superconductor $BaFe_2(As_{0.7}P_{0.3})_2$. *Nat Phys* 2012; **8**: 371.
125. Chu, JH, Analytis, JG and Greve, KD *et al.* In-plane resistivity anisotropy in an underdoped iron arsenide superconductor. *Science* 2010; **329**: 824.
126. Shimojima, T, Sakaguchi, F and Ishizaka, K *et al.* Orbital-independent superconducting gaps in iron pnictides. *Science* 2011; **332**: 564.
127. Lee, CC, Yin, WG and Ku, W. Ferro-orbital order and strong magnetic anisotropy in the parent compounds of iron-pnictide superconductors. *Phys Rev Lett* 2009; **103**: 267001.
128. Chuang, TM, Allan, MP and Lee, JH *et al.* Nematic electronic structure in the 'Parent' state of the iron-based superconductor $Ca(Fe_{1-x}Co_x)_2As_2$. *Science* 2010; **327**: 181.
129. Zhang, Y, He, C and Ye, ZR *et al.* Symmetry breaking via orbital-dependent reconstruction of electronic structure in detwinned NaFeAs. *Phys Rev B* 2012; **85**: 085121.
130. Yi, M, Lu, DH and Chu, JH *et al.* Symmetry-breaking orbital anisotropy observed for detwinned $Ba(Fe_{1-x}Co_x)_2As_2$ above the spin density wave transition. *Proc Natl Acad Sci USA* 2011; **108**: 6878.
131. Hu, JP and Xu, CK. Nematic orders in iron-based superconductors. *Physica C* 2012; **481**: 215–22. *arXiv* 2011;1112.2713.
132. Bao, W, Qiu, Y and Huang, Q *et al.* Tunable ($\delta\pi$, $\delta\pi$)-type antiferromagnetic order in α-Fe(Te,Se) superconductors. *Phys Rev Lett* 2009; **102**: 247001.
133. Ma, FJ, Ji, W and Hu, JP *et al.* First-principles calculations of the electronic structure of tetragonal α-FeTe and α-FeSe crystals: evidence for a bicollinear antiferromagnetic order. *Phys Rev Lett* 2009; **102**: 177003.
134. Li, SL, Cruz, Cdl and Huang, Q *et al.* First-order magnetic and structural phase transitions in $Fe_{1+y}Se_xTe_{1-x}$. *Phys Rev B* 2009; **79**: 054503.
135. Ding, H, Richard, P and Nakayama, K *et al.* Observation of Fermi-surface-dependent nodeless superconducting gaps in $Ba_{0.6}K_{0.4}Fe_2As_2$. *Europhys Lett* 2008; **83**: 47001.
136. Terashima, K, Sekiba, Y and Bowen, JH *et al.* Fermi surface nesting induced strong pairing in iron-based superconductors. *Proc Natl Acad Sci USA* 2009; **106**: 7330.
137. Miao, H, Richard, P and Tanaka, Y *et al.* Isotropic superconducting gaps with enhanced pairing on electron Fermi surfaces in $FeTe_{0.55}Se_{0.45}$. *Phys Rev B* 2012; **85**: 094506.
138. Hashimoto, K, Yamashita, M and Kasahara, S *et al.* Line nodes in the energy gap of superconducting $BaFe_2(As_{1-x}P_x)_2$ single crystals as seen via penetration depth and thermal conductivity. *Phys Rev B* 2010; **81**: 220501.
139. Yamashita, M, Senshu, Y and Shibauchi, T *et al.* Nodal gap structure of superconducting $BaFe_2(As_{1-x}P_x)_2$ from angle-resolved thermal conductivity in a magnetic field. *Phys Rev B* 2011; **84**: 060507.

140. Nakai, Y, Iye, T and Kitagawa, S *et al.* ^{31}P and ^{75}As NMR evidence for a residual density of states at zero energy in superconducting $BaFe_2(As_{0.67}P_{0.33})_2$. *Phys Rev B* 2010; **81**: 020503 (R).
141. Hashimoto, K, Kasahara, S and Katsumata, R *et al.* Nodal versus nodeless behaviors of the order parameters of LiFeP and LiFeAs superconductors from magnetic penetration-depth measurements. *Phys Rev Lett* 2012; **108**: 047003.
142. Qiu, X, Zhou, SY and Zhang, H *et al.* Robust nodal superconductivity induced by isovalent doping in $Ba(Fe_{1-x}Ru_x)_2As_2$ and $BaFe_2(As_{1-x}P_x)_2$. *Phys Rev X* 2012; **2**: 011010.
143. Dong, JK, Zhou, SY and Guan, TY *et al.* Quantum criticality and nodal superconductivity in the FeAs-based superconductor KFe_2As_2. *Phys Rev Lett* 2010; **104**: 087005.
144. Song, CL, Wang, YL and Cheng, P *et al.* Direct observation of nodes and twofold symmetry in FeSe superconductor. *Science* 2011; **332**: 1410.
145. Dong, JK, Zhou, SY and Guan, TY *et al.* Thermal conductivity of overdoped $BaFe_{1.73}Co_{0.27}As_2$ single crystal: evidence for nodeless multiple superconducting gaps and interband interactions. *Phys Rev B* 2010; **81**: 094520.
146. Khasanov, R, Conder, K and Pomjakushina, E *et al.* Evidence of nodeless superconductivity in $FeSe_{0.85}$ from a muon-spin-rotation study of the in-plane magnetic penetration depth. *Phys Rev B* 2008; **78**: 220510.
147. Chi, S, Grothe, S and Liang, RX *et al.* Scanning tunneling spectroscopy of superconducting LiFeAs single crystals: evidence for two nodeless energy gaps and coupling to a bosonic mode. *Phys Rev Lett* 2012; **109**: 087002.
148. Ding, L, Dong, JK and Zhou, SY *et al.* Nodeless superconducting gap in electron-doped $BaFe_{1.9}Ni_{0.1}As_2$ probed by quasiparticle heat transport. *New J Phys* 2009; **11**: 093018.
149. Zhang, Y, Yang, LX and Chen, F *et al.* Out-of-plane Momentum and Symmetry-dependent energy gap of the pnictide $Ba_{0.6}K_{0.4}Fe_2As_2$ superconductor revealed by angle-resolved photoemission spectroscopy. *Phys Rev Lett* 2010; **105**: 117003.
150. Kuroki, K, Onari, S and Arita, R *et al.* Unconventional pairing originating from the disconnected Fermi surfaces of superconducting $LaFeAsO_{1-x}F_x$. *Phys Rev Lett* 2008; **101**: 087004.
151. Mazin, II, Singh, DJ and Johannes, MD *et al.* Unconventional superconductivity with a sign reversal in the order parameter of $LaFeAsO_{1-x}F_x$. *Phys Rev Lett* 2008; **101**: 057003.
152. Hanaguri, T, Niitaka, S and Kuroki, K *et al.* Unconventional s-wave superconductivity in Fe(Se,Te). *Science* 2010; **328**: 474–6.
153. Suzuki, K, Usui, H and Kuroki, K. Possible three-dimensional nodes in the $s_{\pm}$ superconducting gap of $BaFe_2(As_{1-x}P_x)_2$. *J Phys Soc Jpn* 2011; **80**: 013710.
154. Okazaki, K, Ota, Y and Kotani, Y *et al.* Octet-line node structure of superconducting order parameter in KFe_2As_2. *Science* 2012; **337**: 1314–7.
155. Xu, N, Richard, P and Shi, X *et al.* Possible nodal superconducting gap and Lifshitz transition in heavily hole-doped $Ba_{0.1}K_{0.9}Fe_2As_2$. *Phys Rev B* 2013; **88**: 220508 (R).
156. Drew, AJ, Niedermayer, C and Baker, PJ *et al.* Coexistence of static magnetism and superconductivity in $SmFeAsO_{1-x}F_x$ as revealed by muon spin rotation. *Nat Mater* 2009; **8**: 310–4.
157. Fernandes, RM, Pratt, DK and Tian, W *et al.* Unconventional pairing in the iron arsenide superconductors. *Phys Rev B* 2010; **81**: 140501.
158. Chen, H, Ren, Y and Qiu, Y *et al.* Coexistence of the spin-density wave and superconductivity in $Ba_{1-x}K_xFe_2As_2$. *Europhys Lett* 2009; **85**: 17006.
159. Ge, QQ, Ye, ZR and Xu, M *et al.* Anisotropic but nodeless superconducting gap in the presence of spin-density wave in iron-pnictide superconductor $NaFe_{1-x}Co_xAs$. *Phys Rev X* 2013; **3**: 011020.
160. Zhang, Y, Wei, J and Ou, HW *et al.* Unusual doping dependence of the electronic structure and coexistence of spin-density-wave and superconductor phases in single crystalline $Sr_{1-x}K_xFe_2As_2$. *Phys Rev Lett* 2009; **102**: 127003.
161. Cai, P, Zhou, XD and Ruan, W *et al.* Visualizing the microscopic coexistence of spin density wave and superconductivity in underdoped $NaFe_{1-x}Co_xAs$. *Nat Commun* 2013; **4**: 1596.
162. Parker, D, Vavilov, MG and Chubukov, AV *et al.* Coexistence of superconductivity and a spin-density wave in pnictide superconductors: gap symmetry and nodal lines. *Phys Rev B* 2009; **80**: 100508 (R).
163. Maiti, S, Fernandes, RM and Chubukov, AV. Gap nodes induced by coexistence with antiferromagnetism in iron-based superconductors. *Phys Rev B* 2012; **85**: 144527.
164. Liu, C, Palczewski, AD and Dhaka, RS *et al.* Importance of the Fermi-surface topology to the superconducting state of the electron-doped pnictide $Ba(Fe_{1-x}Co_x)_2As_2$. *Phys Rev B* 2011; **84**: 020509 (R).
165. Shen, XP, Chen, SD and Ge, QQ *et al.* Electronic structure of $Ca_{10}(Pt_4As_8)(Fe_{2-x}Pt_xAs_2)_5$ with metallic Pt_4As_8 layers: an angle-resolved photoemission spectroscopy study. *Phys Rev B* 2013; **88**: 115124.
166. Li, J, Guo, YF and Zhang, SB *et al.* Superconductivity suppression of $Ba_{0.5}K_{0.5}Fe_{2-2x}M_{2x}As_2$ single crystals by substitution of transition metal (M = Mn, Ru, Co, Ni, Cu, and Zn). *Phys Rev B* 2012; **85**: 214509.
167. Suzuki, H, Yoshida, T and Ideta, S *et al.* Absence of superconductivity in the hole-doped Fe pnictide $Ba(Fe_{1-x}Mn_x)_2As_2$: photoemission and x-ray absorption spectroscopy studies. *Phys Rev B* 2013; **88**: 100501 (R).
168. Hu, JP and Ding, H. Local antiferromagnetic exchange and collaborative Fermi surface as key ingredients of high temperature superconductors. *Sci Rep* 2012; **2**: 381.
169. He, SL, He, JF and Zhang, WH *et al.* Phase diagram and electronic indication of high-temperature superconductivity at 65 K in single-layer FeSe films. *Nat Mater* 2013; **12**: 605–10.
170. Chen, F, Xu, M and Ge, QQ *et al.* Electronic identification of the parental phases and mesoscopic phase separation of $K_xFe_{2-y}Se_2$ superconductors. *Phys Rev X* 2011; **1**: 021020.
171. Li, W, Ding, H and Deng, P *et al.* Phase separation and magnetic order in K-doped iron selenide superconductor. *Nat Phys* 2012; **8**: 126–30.
172. Wang, Z, Song, YJ and Shi, HL *et al.* Microstructure and ordering of iron vacancies in the superconductor system $K_yFe_xSe_2$ as seen via transmission electron microscopy. *Phys Rev B* 2011; **83**: 140505 (R).
173. Ricci, A, Poccia, N and Campi, G *et al.* Nanoscale phase separation in the iron chalcogenide superconductor $K_{0.8}Fe_{1.6}Se_2$ as seen via scanning nanofocused x-ray diffraction. *Phys Rev B* 2011; **84**: 060511.
174. Xu, M, Ge, QQ and Peng, R *et al.* Evidence for an s-wave superconducting gap in $K_xFe_{2-y}Se_2$ from angle-resolved photoemission. *Phys Rev B* 2012; **85**: 220504.
175. Park, JT, Friemel, G and Li, Y *et al.* Magnetic resonant mode in the low-energy spin-excitation spectrum of superconducting $Rb_2Fe_4Se_5$ single crystals. *Phys Rev Lett* 2011; **107**: 177005.
176. Peng, R, Shen, XP and Xie, X *et al.* Enhanced superconductivity and evidence for novel pairing in single-layer FeSe on $SrTiO_3$ thin film under large tensile strain. *Phys Rev Lett* 2013; **112**: 107001. *arXiv* 2013; 1310.3060.
177. Hu, JP. Iron-based superconductors as odd-parity superconductors. *Phys Rev X* 2013; **3**: 031004.
178. Peng, R, Xu, HC and Tan, SY *et al.* Critical role of substrate in the high temperature superconductivity of single layer FeSe on Nb:$BaTiO_3$. *arXiv* 2014; 1402.1357.

179. Yin, WG, Lee, CC and Ku, W. Unified picture for magnetic correlations in iron-based superconductors. *Phys Rev Lett* 2010; **105**: 107004.
180. Yin, ZP, Haule, K and Kotliar, G. Kinetic frustration and the nature of the magnetic and paramagnetic states in iron pnictides and iron chalcogenides. *Nat Mater* 2011; **10**: 932–5.
181. Jiang, J, He, C and Zhang, Y *et al.* Distinct in-plane resistivity anisotropy in a detwinned FeTe single crystal: evidence for a Hund's metal. *Phys Rev B* 2013; **88**: 115130.
182. Kaneko, K, Hoser, A and Caroca-Canales, N *et al.* Columnar magnetic structure coupled with orthorhombic distortion in the antiferromagnetic iron arsenide $SrFe_2As_2$. *Phys Rev B* 2008; **78**: 212502.
183. Xiao, Y, Su, Y and Meven, M *et al.* Magnetic structure of $EuFe_2As_2$ determined by single-crystal neutron diffraction. *Phys Rev B* 2009; **80**: 174424.
184. Goldman, AI, Argyriou, DN and Ouladdiaf, B *et al.* Lattice and magnetic instabilities in $CaFe_2As_2$: a single-crystal neutron diffraction study. *Phys Rev B* 2008; **78**: 100506.
185. Chen, Y, Lynn, JW and Li, J *et al.* Magnetic order of the iron spins in NdFeAsO. *Phys Rev B* 2008; **78**: 064515.
186. Wilson, SD, Yamani, Z and Rotundu, CR *et al.* Neutron diffraction study of the magnetic and structural phase transitions in $BaFe_2As_2$. *Phys Rev B* 2009; **79**: 184519.
187. Zhao, J, Huang, Q and Cruz, DL *et al.* Lattice and magnetic structures of PrFeAsO, $PrFeAsO_{0.85}F_{0.15}$, and $PrFeAsO_{0.85}$. *Phys Rev B* 2008; **78**: 132504.
188. Lester, C, Chu, JH and Analytis, JG *et al.* Neutron scattering study of the interplay between structure and magnetism in $Ba(Fe_{1-x}Co_x)_2As_2$. *Phys Rev B* 2009; **79**: 144523.
189. Park, JT, Inosov, DS and Niedermayer, C *et al.* Electronic phase separation in the slightly underdoped iron pnictide superconductor $Ba_{1-x}K_xFe_2As_2$. *Phys Rev Lett* 2009; **102**: 117006.
190. Li, SL, Cruz, CDL and Huang, Q *et al.* Structural and magnetic phase transitions in $Na_{1-\delta}FeAs$. *Phys Rev B* 2009; **80**: 020504.
191. Lee, JJ, Schmitt, FT and Moore, RG *et al.* Evidence for pairing enhancement in single unit cell FeSe on $SrTiO_3$ due to cross-interfacial electron-phonon coupling. *arXiv* 2014; 1312.2633.
192. McMillan, WL. Transition temperature of strong-coupled superconductors. *Phys Rev* 1968; **167**: 331.
193. Ma, F, Lu, ZY and Xiang, T. Main nteractions in ron-based superconductors. *Front Phys China* 2010; **5**: 150.
194. Yildirim, T. Origin of the 150-K anomaly in LaFeAsO: competing antiferromagnetic interactions, frustration, and a structural phase transition. *Phys Rev Lett* 2008; **101**: 057010.
195. Ma, F, Lu, ZY and Xiang, T. Arsenic-bridged antiferromagnetic superexchange interactions in LaFeAsO. *Phys Rev B* 2008; **78**: 224517.
196. Liu, K, Lu, ZY and Xiang, T. Atomic and electronic structures of FeSe monolayer and bilayer thin films on $SrTiO_3$ (001): first-principles study. *Phys Rev B* 2012; **85**: 235123.
197. Liu, D, Zhang, WH and Mou, DX *et al.* Electronic origin of high-temperature superconductivity in single-layer FeSe superconductor. *Nat Commun* 2012; **3**: 931.
198. Bao, W, Huang, QZ and Chen, GF *et al.* A novel large moment antiferromagnetic order in $K_{0.8}Fe_{1.6}Se_2$ superconductor. *Chin Phys Lett* 2011; **28**: 086104.
199. Kou, SP, Li, T and Weng, ZY. Coupled local moments and itinerant electrons in iron-based superconductors. *Europhys Lett* 2009; **88**: 17010.
200. Si, Q and Abrahams, E. Strong correlations and magnetic frustration in the high T_c iron pnictides. *Phys Rev Lett* 2008; **101**: 076401.
201. Seo, K, Bernevig, BA and Hu, J. Pairing symmetry in a two-orbital exchange coupling model of oxypnictides. *Phys Rev Lett* 2008; **101**: 206404.
202. Wang, F, Zhai, H and Ran, Y *et al.* Functional renormalization-group study of the pairing symmetry and pairing mechanism of the FeAs-based high-temperature superconductor. *Phys Rev Lett* 2009; **102**: 047005.
203. Kuroki, K, Usui, H and Onari, S *et al.* Pnictogen height as a possible switch between high-T_c nodeless and low-T_c nodal pairings in the iron-based superconductors. *Phys Rev B* 2009; **79**: 224511.
204. Chen, WQ, Yang, KY and Zhou, Y *et al.* Strong coupling theory for superconducting iron pnictides. *Phys Rev Lett* 2009; **102**: 047006.
205. Onari, S and Kontani, H. Violation of Anderson's theorem for the sign-reversing s-wave state of iron-pnictide superconductors. *Phys Rev Lett* 2009; **103**: 177001.
206. Chen, WQ, Ma, FJ and Lu, ZY *et al.* π-junction to probe antiphase s-wave pairing in iron pnictide superconductors. *Phys Rev Lett* 2009; **103**: 207001.
207. Inosov, DS, Park, JT and Bourges, P *et al.* Normal-state spin dynamics and temperature-dependent spin-resonance energy in optimally doped $BaFe_{1.85}Co_{0.15}As_2$. *Nat Phys* 2010; **6**: 178–81.
208. Li, S, Zhang, C and Wang, M *et al.* Normal-state hourglass dispersion of the spin excitations in $FeSe_xTe_{1-x}$. *Phys Rev Lett* 2010; **105**: 157002.
209. Li, YK, Tong, J and Tao, Q *et al.* Effect of a Zn impurity on T_c and its implications for pairing symmetry in $LaFeAsO_{1-x}F_x$. *New J Phys* 2010; **12**: 083008.
210. Fernandes, RM and Schmalian, J. Competing order and nature of the pairing state in the iron pnictides. *Phys Rev B* 2010; **82**: 014521.
211. Laplace, Y, Bobroff, J and Rullier-Albenque, F *et al.* Atomic coexistence of superconductivity and incommensurate magnetic order in the pnictide $Ba(Fe_{1-x}Co_x)_2As_2$. *Phys Rev B* 2009; **80**: 140501.
212. Zhang, Y and Feng, DL. Angle-resolved photoemission spectroscopy study on iron-based superconductors. *AAPPS Bull* 2012; **22**: 2.
213. Ye, ZR, Zhang, Y and Xie, BP *et al.* Angle-resolved photoemission spectroscopy study on iron-based superconductors. *Chin Phys B* 2013; **22**: 087407.
214. Umezawa, K, Li, Y and Miao, H *et al.* Unconventional anisotropic s-wave superconducting gaps of the LiFeAs iron-pnictide superconductor. *Phys Rev Lett* 2012; **108**: 037002.
215. Medvedev, S, MacQueen, TM and Troyan, IA *et al.* Electronic and magnetic phase diagram of β-$Fe_{1.01}Se$ with superconductivity at 36.7 K under pressure. *Nat Mater* 2009; **8**: 630–3.